

https://dspace.org/

Melt breccias in parautochthonous basement rocks of the Morokweng impact structure South Africa Evidence for a friction origin

Roger Gibson; Slindile Wela; Leonidas Vonopartis; Marco Andreoli

PERGAMON-ELSEVIER SCIENCE LTD
https://hdl.handle.net/10539/40820
WOS

Downloaded from a DSpace repository. https://dspace.org/

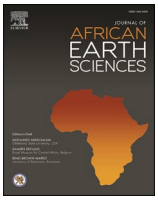
Journal of African Earth Sciences 214 (2024) 105239



Contents lists available at ScienceDirect

Journal of African Earth Sciences

journal homepage: www.elsevier.com/locate/jafrearsci





Melt breccias in parautochthonous basement rocks of the Morokweng impact structure, South Africa – Evidence for a friction origin

Roger L. Gibson *, S'lindile S. Wela, Leonidas C. Vonopartis, Marco A.G. Andreoli

School of Geosciences, University of the Witwatersrand, PO WITS, Johannesburg 2050, South Africa

ARTICLE INFO

Handling Editor: Dr. Mohamed Mohamed G. Abdelsalam

Keywords:
Cataclasite
Friction melting
Impact crater
Morokweng
Peak ring
Pseudotachylite

ABSTRACT

Archaean granitoid gneisses and younger metadolerite and dolerite intrusions in a drill core from the late-Jurassic Morokweng impact structure, host mm- to m-wide aphanitic dykes that are spatially and geometrically associated with cataclasite-bearing reverse-slip faults. The dykes contain lithic and mineral clasts derived from their wallrocks. Petrographic and BSEM analysis indicates that the original dyke matrices are completely altered to a smectite-zeolite-magnetite paragenesis. However, a melt precursor is argued based on evidence for low-viscosity flow, high dyke aspect ratios and intrusive relationships into both the wallrocks and cataclasite, and the sharply contrasting matrix hydrothermal mineral grain size and textures relative to those found in the cataclasites. A subset of cm-wide pink-orange monomictic dykes have a felsic composition closely resembling their granitic wallrocks. More voluminous, polymictic, red dykes show compositions intermediate between the mafic and felsic wallrock endmembers in the drill core, which both occur in close proximity to the dykes. These hybrid compositions are interpreted to have developed either through mixing of mafic and felsic melts along faulted contacts between the doleritic and gneissic rocks, or by mechanical mixing, with or without assimilation, of a dolerite-derived melt with incohesive granitoid-derived cataclasite within the fault zones. The structural, petrographic and geochemical evidence support the dykes originating by friction melting (pseudotachylite, s.s.) caused by high-strain-rate faulting of the crater basement during the excavation and/or modification stages of the Morokweng impact, rather than by contamination of impact melt intrusions. Based on their spatial context relative to the impact melt sheet and the moderately high shock levels of their host rocks, these pseudotachylite dykes are interpreted as part of the parautochthonous peak ring of the Morokweng impact structure.

1. Introduction

The rapid transfer of exceptional amounts of kinetic energy from an impacting bolide into target crust can generate melts on a variety of scales through disparate mechanisms (French, 1998; Osinski et al., 2013; Spray and Biren, 2021). Of these, rapid decompression of rocks subjected to shock pressures exceeding 60 GPa near the point of impact leads to the generation of substantial volumes of impact melt (Grieve et al., 1977) that mainly overlies - but can also intrude significant distances into - the subjacent fractured and brecciated crater basement (Reimold and Gibson, 2005; Kenkmann et al., 2014; Spray and Biren, 2021). Within this basement, but still within the shocked rock volume, local shock pressure excursions may additionally create discrete, limited volume, (par)autochthonous shock melt dykes similar to those reported in many meteorites (Biren and Spray, 2011). Finally, frictional sliding along faults accommodating complex, high strain rate, movements in the crater basement as it adjusts towards the final crater form after the initial shock pulse can produce friction melts (pseudotachylite) in both shocked and unshocked rocks (Reimold, 1995; Reimold and Gibson, 2005; Spray and Biren, 2021). Identifying the precise origin of melts in impact structures thus provides important insights into cratering dynamics and, where craters have been substantially eroded, dyke geometries and distribution may also assist in constraining crater dimensions and erosion level. However, interpretation can be complicated by, inter alia, (a) the highly brecciated and disrupted nature of the crater basement, (b) the extreme spatial and temporal variability in impact stress and strain patterns on timescales of seconds to minutes, (c) the large and complex vertical and/or horizontal movements accompanying the excavation and modification stages of crater formation that can severely modify and/or disrupt initial relationships (e.g., Thompson and Spray, 2017), and (d) post-impact annealing and/or hydrothermal effects in the crater basement that may overprint, modify and possibly even destroy

* Corresponding author.
E-mail address: roger.gibson@wits.ac.za (R.L. Gibson).

https://doi.org/10.1016/j.jafrearsci.2024.105239
Received 29 December 2023; Received in revised form 7 March 2024; Accepted 22 March 2024
Available online 29 March 2024
1464-343X/© 2024 The Authors. Published by Elsevier Ltd. This is an open access article under the CC BY-NC license (http://creativecommons.org/licenses/by-nc/4.0/).

key microscopic evidence (e.g., Reimold and Gibson, 2005; Spray and Biren, 2021). The similar gross outward appearance of the three melt types – especially when hydrothermally altered - which generally manifest as aphanitic clast-bearing sheet-like (dyke or sill) bodies (e.g., Hall and Molengraaff, 1925; Lightfoot et al., 1997; Riller et al., 2018; De Graaff et al., 2021; Spray and Biren, 2021) also presents challenges in differentiating between them and in constraining their genesis.

This study investigates the origin of a suite of mm- to m-wide monomictic to polymictic clast-bearing aphanitic dykes (Figs. 2 and 3) intersected in a 369 m long vertical drill core (designated M4) located ~18 km from the estimated centre of the Morokweng impact structure (MIS) in northwestern South Africa. The MIS exhibits one of the thickest preserved impact-melt sheets on Earth (Hart et al., 2002; Kenny et al., 2021). In this paper we demonstrate that these aphanitic breccia dykes in the M4 drill core differ from the impact-melt rock intersected in other cores closer to the centre of the MIS. We interpret them as friction melts (pseudotachylite) formed during high-strain-rate slip in the crater basement associated with the crater excavation and/or modification stages of the Morokweng impact.

2. Geological setting

The Morokweng impact structure (MIS) is a partially eroded hypervelocity impact crater remnant situated in Neoarchaean granite-greenstone rocks that form the western part of the Kaapvaal craton (Gibson et al., 2022; Fig. 1). Owing to a cover sequence of Late Cretaceous to Cenozoic Kalahari Group sediments, its existence has been established only through the identification of shock microdeformation effects in quartz grains in samples recovered from borehole cores drilled through the thin (≤200 m) sedimentary veneer (Andreoli et al., 1995; Corner et al., 1997; Hart et al., 1997; Reimold et al., 1999; Gibson et al., 2024). The MIS has a minimum apparent diameter of ~70 km (Henkel

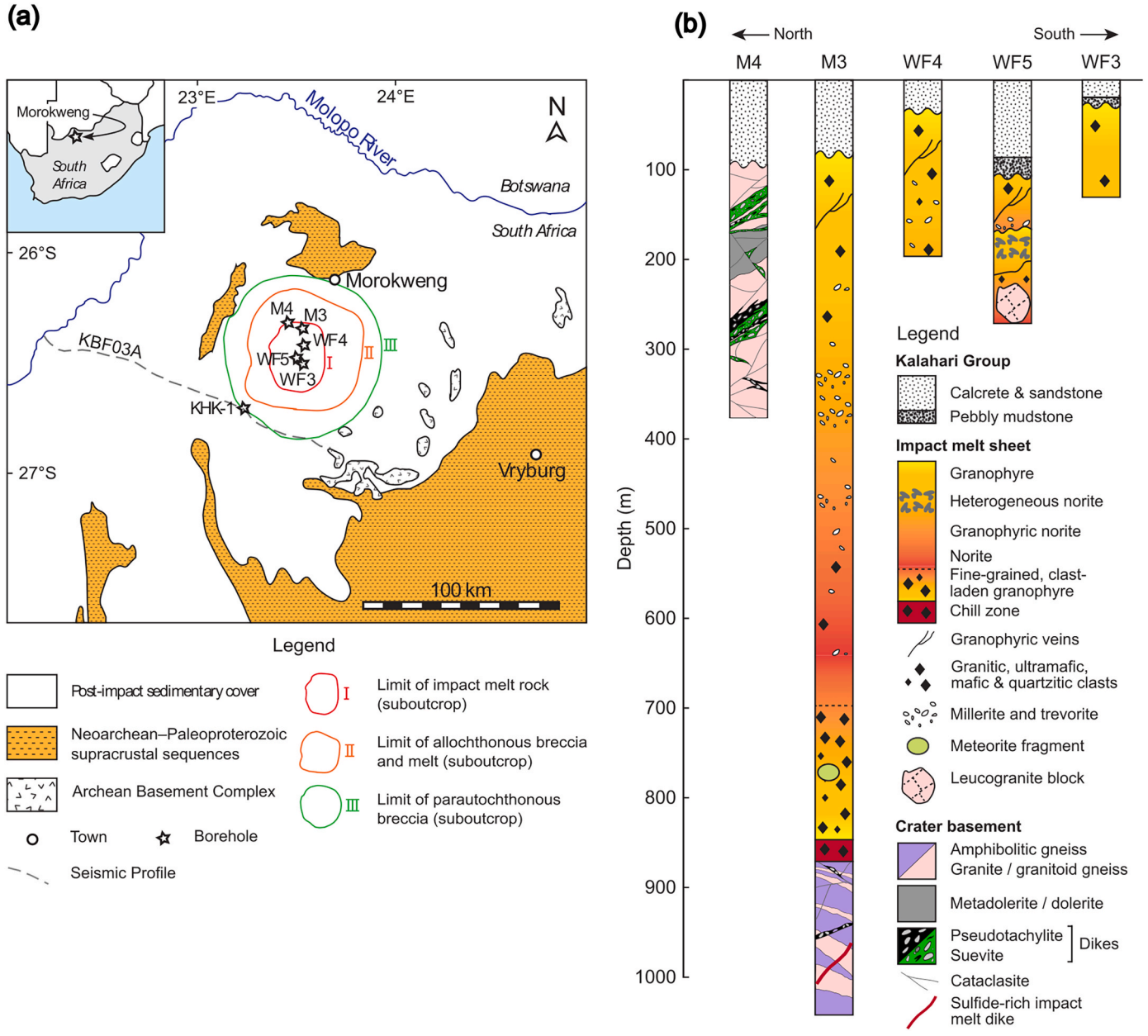


Fig. 1. Geological context of the M4 drill core. (a) Simplified geological map of the buried Morokweng impact structure showing the interpreted limits of the principal geophysical features (modified after Hart et al., 2002) and locations of the principal boreholes referred to in the text. (b) Simplified logs of the principal exploration drill cores from the central parts of the MIS (modified after Hart et al. (2002) and Wela (2017)).

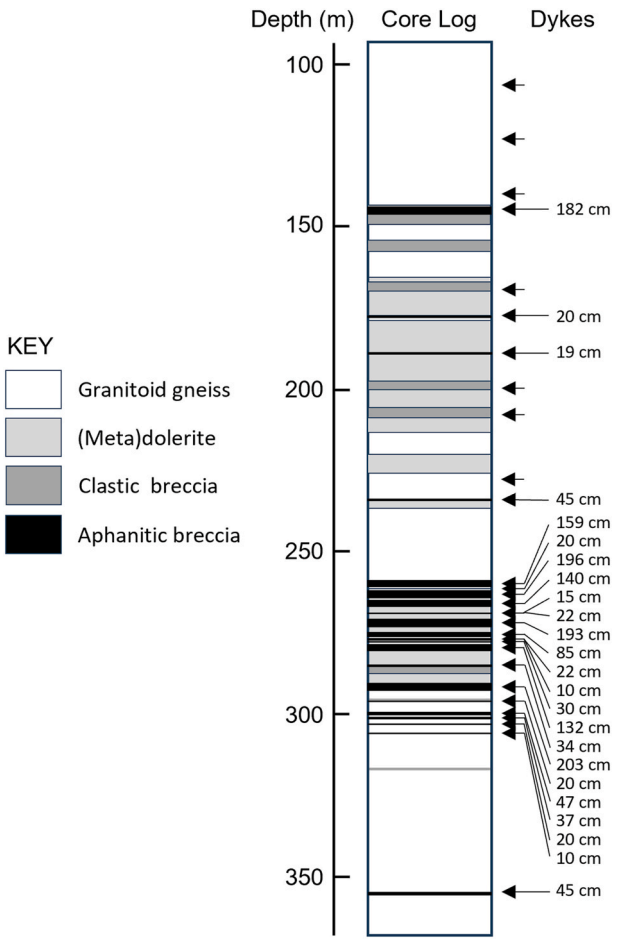


Fig. 2. Simplified lithological log of the crater basement section of the M4 drill core showing the locations of clastic-matrix and aphanitic breccia dykes. Thicknesses of aphanitic dykes ≥10 cm are listed; short arrows indicate intersections of aphanitic dykes with thicknesses of 1–10 cm.

et al., 2002) based on interpretation of a circular magnetic anomaly comprising an inner, ~30 km diameter, ≤350 nT, positive anomaly that is surrounded by an ~20 km wide annulus in which the regional magnetic dyke pattern is subdued and disrupted (Corner et al., 1997). Gibson et al. (2024) have proposed an original crater rim diameter of between 70 and 80 km based on numerical modelling.

The inner magnetic anomaly in the MIS has been interpreted by Henkel et al. (2002) as reflecting the extent of a >500 m thick impact melt sheet, confirmation of which has been provided by four exploration boreholes (Fig. 1). Of these, only the M3 hole reached the crater basement, establishing a minimum, post-erosion, melt sheet thickness of ~800 m. Based on zircon geochronometry, Kenny et al. (2021) proposed a pre-erosion melt sheet thickness of ~1.1 km. The impact-melt rock has a broadly quartz norite composition with a phaneritic, medium- to coarse-grained, granophyric texture and contains lithic clasts of dolerite, gabbro, amphibolite, granite, quartzite, and serpentinised ultramafic rock (Hart et al., 1997, 2002; Koeberl et al., 1997; McDonald et al., 2001; Koeberl and Reimold, 2003; Kenny et al., 2021). The melt sheet is differentiated (Kenny et al., 2021). The lower part of the melt sheet in the M3 drill core is texturally highly heterogeneous and clast-rich, with an aphanitic, microcrystalline texture along the footwall contact. The impact melt rock is highly unusual both in its elevated meteorite-derived geochemical component (up to 5 wt%; Koeberl et al., 2002) and in the retention of relict meteorite fragments (Maier et al., 2006). The impact age of 146 Ma was established independently from authigenic zircons in the impact melt by Hart et al. (1997), Koeberl et al. (1997) and Kenny et al. (2021).

The M4 borehole site lies 6 km WNW of the M3 drill site, immediately outside the limits of the central magnetic anomaly that Henkel et al. (2002) associate with the impact melt sheet (Fig. 1a). It intersected a significantly different lithological association to the more centrally situated drill cores, which is described in Wela (2017) and Gibson et al. (2022, 2024, this paper) (Fig. 1b).

3. Methodology

The 368.58 m long, 4.6 cm diameter, M4 borehole was drilled in 1998–1999 by Business Venture Investments no. 33 (Pty) Ltd into a small magnetic anomaly ~18 km NNW from the inferred centre of the MIS (26° 29′ 32″S, 23° 34′ 33″E; Fig. 1) as part of an exploration programme for base metal mineralization. The upper 94 m of Kalahari Group sand and calcrete was discarded. The remaining core was initially logged informally as MOROK 5 by M.A.G. Andreoli (unpublished company report) and then re-logged by Wela (2017; Fig. 2) to identify principal rock types and significant structural (faults, cataclasite/-breccia zones and melt dykes) and alteration features (veins, vugs, alteration zones), from which samples were selected for further petrographic and geochemical analysis.

A total of 98 thin sections were prepared as part of the investigation by Wela (2017) for mineral and textural petrographic analysis, including transmitted and reflected light microscopy using a Leica DM-LSP microscope, and backscattered electron microscopy (BSEM) using a Tescan Vega 3 LM SEM equipped with an energy dispersive spectrometer and using Aztec software at the Spectrum Analytical Facility (SPECTRAU), at the University of Johannesburg, operating at 30 kV.

Bulk geochemical analysis was performed on 14 aphanitic dyke, 26 granitoid and 8 dolerite samples; the granitoid target rock data were reported in Gibson et al. (2022) but are repeated here for completeness. Representative bulk compositions of the target rocks were obtained by sampling up to 1 m intersections of halved core; for the aphanitic dyke samples, lithic-clast-poor half-core intersections of between 5 and 20 cm were used, depending on individual dyke widths. For obvious reasons, thinner dykes could not be analysed in this way.

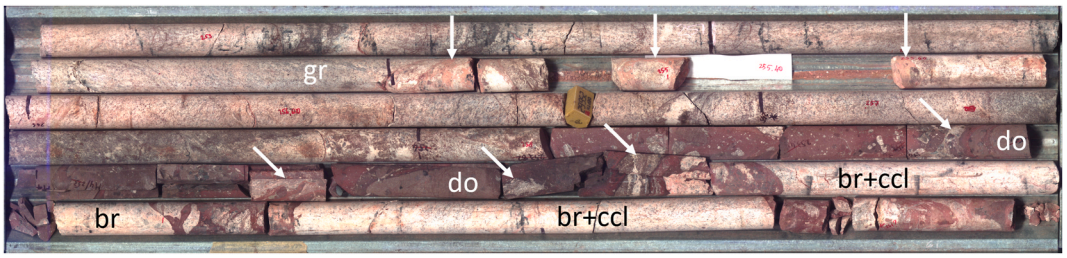


Fig. 3. Core tray through the upper contact of the main aphanitic dyke interval in the M4 drill core, from 254.2 to 262.6 m depth. Depth increases from top left to bottom right, core tray length is 1.5 m. The granitoid gneisses (gr) are faulted, cataclased (ccl) and locally brecciated (br). Felsic orange aphanitic dykes up to several cm wide (vertical arrows) occur between 254.5 and 255.4 m depth and contain only granite gneiss clasts (monomictic). The main aphanitic dyke (1.8 m width) is red-brown, polymictic and contains cm- to dm-wide granitic and doleritic (do) clasts and cataclasite masses (diagonal arrows).

Samples for X-ray fluorescence (XRF) and inductively coupled plasma mass spectrometry (ICP-MS) were prepared and processed in the Earth Lab, School of Geosciences at the University of the Witwatersrand (UW), according to procedures outlined in Wilson (2012). The samples were initially crushed in a carbon steel jaw crusher and subsequently milled in a carbon-steel swing mill. For major elements, 0.34 g of powdered sample was fused at 1100 °C using Johnson Matthey Spectroflux 105, and 50 μg of powdered sample was digested by the open beaker/hot plate method. Major elements were analysed using a Panalytical Axios Max XRF spectrometer, with raw data correction done through proprietary software. Standard calibrations used synthetic oxide blends, internationally recognised rock standards, and internal quality controls. Calibration standards included primary USGS International Reference Materials and the NIM series (South Africa) which include NIM-P, NIM-D, W2, NIM-S, GSP2, BCR2, NIM-N, NIM-G, PCC1, BHVO2, AGV2, G2, DTS1. Trace element analysis was conducted utilising the Perkin Elmer DRC-e inductively coupled plasma mass spectrometer (ICP-MS) and compared against certified primary solution standards. International reference materials (BCR1, BHVO1 and BIR1) were analysed with each run for quality control. The standard range for ICP-MS analysis was 10–100 ppb but the samples were diluted 1000 times. The lower limits of detection of all elements for the XRF and ICP-MS analyses are 0.01 % and 0.01 ppm, respectively. The major and trace element compositions for the samples are presented in Tables 1–3.

A half-core section through a single dyke was scanned using a Bruker M4 Tornado micro-XRF (μXRF) at Sci-Ba Laboratories in Cape Town to investigate internal chemical variation within the dykes. Although not reported here, Wela (2017) confirmed the principal alteration mineralogy (smectite, zeolite) in the dykes via electron probe micro-analyser (EPMA) and bulk powder X-ray diffraction (XRD) analysis.

4. Lithological, shock and alteration features of the M4 core

The M4 hole intersected Late Cretaceous to Cenozoic clastic sediments and calcrete to a depth of 94 m. Highly weathered granitoid rock, to a depth of 103 m, was recovered by percussion drilling and was too deteriorated to analyse. The remainder of the hole, between 103 and 369 m, intersected heterogeneous granitoid gneisses (70%) with subsidiary mafic intrusive rocks (18%) that are all cut by cataclasite-bearing faults and dyke breccias with either clastic or aphanitic matrices that together constitute the remaining 12% (Wela, 2017).

The medium- to coarse-grained granitoid gneisses (granite, granodiorite, trondhjemite, monzonite) represent a Neoarchaean calc-alkaline TTG suite of 2.91–2.92 Ga age (Gibson et al., 2022). The granitoid gneisses comprise predominantly quartz and plagioclase (alkali feldspar is significant only in the granitic varieties) with <5 vol% biotite. Accessory minerals include epidote, titanite, (titano)magnetite and apatite. The monzonite variety differs from the other granitoid gneisses in containing up to 15 vol% biotite, with epidote and titanite reaching several vol%. Gibson et al. (2022) interpreted the granitoid gneisses as tectonised syn- to late-kinematic intrusions emplaced during an upper amphibolite facies dynamothermal metamorphic event linked to collision and amalgamation of two major continental fragments that together constitute the main bulk of the Kaapvaal craton.

Two types of hypabyssal mafic rock occur in the drill core (Fig. 2): metadolerite is the dominant lithology at 166–206 m depth, and alternates with granitoid gneisses between 208 and 236 m, where contacts are defined by cataclasite or breccia. Dolerite occurs in several dm- to m-scale intersections within the cataclasite- and melt-rich breccia zone between 259 m and 296 m depth (Fig. 2). Based on bulk rock geochemical differences, Wela (2017) suggested that the metadolerite intruded during the ca. 2.8 Ga Ventersdorp LIP (large igneous province), and the dolerite during the ca. 1.1 Ga Umkhondo LIP event. The grade of metamorphism in the metadolerite does not appear to have exceeded upper greenschist facies (actinolite-albite-chlorite-quartz-titanite assemblage) and may have been associated with localised faulting and hydrothermal quartz-dominated veining that predated the impact (Wela, 2017). Although affected by significant post-impact hydrothermal alteration, the dolerite retains its subophitic igneous texture comprising plagioclase and clinopyroxene, with no conclusive evidence of any pre-impact metamorphic alteration (Wela, 2017). It contains limited amounts of quartz, biotite, and ilmenite.

Both the granitoid and doleritic lithologies are cut by cataclasite-filled faults and two types of clast-bearing dykes (Figs. 3 and 4). The dykes with a clastic matrix are described in a companion paper and are thus not discussed further here. The second dyke type, which is characterised by an aphanitic matrix that contains evidence of having undergone laminar to turbulent flow, is the subject of this study.

Shock microdeformation features in the gneisses and dolerite include decorated planar deformation features (PDFs), planar fractures, feather features and toasting in quartz, and planar features in plagioclase (Wela, 2017; Gibson et al., 2024). Statistical analysis of decorated PDF orientations in quartz in the granitoid gneisses reveals a relatively uniform peak shock pressure of ~16 GPa throughout the M4 drill core, with no detectable variation in intensity in the vicinity of the main breccia intersections, and an apparent lack of higher-order PDF orientations in clasts in the breccias, which Gibson et al. (2024) suggest may be a consequence of annealing recrystallization and hydrothermal alteration.

Evidence of alteration is found throughout the core and includes fluid inclusion trails along PDF orientations in quartz, extensive sericitisation and clouding of feldspars and oxidation of mafic, Fe–Ti oxide and sulphide minerals in the host rocks. However, it is most pronounced in the cataclasite and breccia dykes, where it may be associated with vugs and/or core loss. Fault surfaces are characterised by smectite clays and/or iron oxides/hydroxides; these are in turn cut by mm- to cm-wide calcite, zeolite and/or anhydrite veins that are more prominent in the upper parts of the core. Alteration mineralogy is dominated by zeolites and smectites but also locally includes chlorite, calcite, actinolite, titanite, alkali feldspar, pyrite, andraditic garnet, anhydrite, and/or magnetite or haematite (Wela, 2017; T. Masiu, pers. comm., 2023).

5. Structures

The limitation of any structural analysis of a vertical, small diameter drill core is that any orientation and spacing measurements will be statistically biased towards subhorizontal features; conversely, analysis of dyke-wallrock relationships could be disproportionately biased towards small-volume dykes with steep orientations that expose a proportionally larger length of the dyke contacts.

The granitoid gneisses that constitute the bulk of the M4 drill core are moderately to weakly foliated and lithologically heterogeneous, comprising a banded gneiss package with both sharp and gradational contacts (Gibson et al., 2022). The dm- to m-scale gneissose layering is parallel to the foliation and both are somewhat sinuous and generally steeply oriented. The original contacts between the metadolerite and the gneisses are typically obscured by faults, dykes and/or alteration zones. The dolerite intersections between 263 and 296 m depth may represent discrete blocks within the widest interval of dykes (Fig. 2), although alternative interpretations are described below. The granitoid gneisses and metadolerite between 208 and 236 m depth show evidence of brittle-ductile protomylonitization in the form of nascent monoclinic shape fabrics and evidence of dynamic recrystallization (bulging grain boundaries and subgrains) in quartz in the gneisses, and angular quartz vein networks infilling stockwork breccia. The presence in the vein quartz of decorated PDFs, aphanitic dykes cross-cutting the veins (Fig. 4a), and inclusion of vein quartz clasts in the dykes, indicate that the mylonitization, brecciation and veining predated the impact.

5.1. Macroscopic impact-related structures

Impact-related faults in the M4 drill core can be identified based on their relationships to other impact-related features. Impact-related

Table 1
Whole-rock compositions of the granitoid gneisses from the M4 drill core. Major elements by XRF analysis are provided in weight percent and trace elements by ICP-MS are provided in parts per million.

Lithology	Granitic gneiss						Trondhjemitic gneiss				Granodioritic gneiss		
Sample #	M4 GG-2	M4 GG-6	M4 GG-17	M4 GG-3	M4 GG-14	M4 GG-15	M4 FZ-2	M4 FZ-3	M4 FZ-4	M4 FZ-1	M4 GG-4	M4 GG-7	M4 GG-8
SiO_2 (wt %)	75.3	74.3	73.6	72.8	74.1	74.8	80.5	75.9	75.8	76.3	72.1	73.3	71.5
TiO_2	0.04	0.05	0.15	0.16	0.18	0.12	0.2	0.2	0.19	0.21	0.31	0.18	0.24
Al_2O_3	14.1	14.6	14.7	14.5	14.1	14.1	10.8	13.6	13.9	13.5	15.1	14.6	15.4
FeO^{tot}	0.71	0.98	1.35	1.65	1.42	1.18	1.07	1.20	1.03	1.1	2.29	1.49	1.82
MnO	0.01	0.01	0.02	0.03	0.01	0.01	0.01	0.01	0.01	0.01	0.02	0.01	0.02
MgO	0.11	0.07	0.42	0.44	0.41	0.33	0.68	0.94	0.66	0.68	0.65	0.39	0.72
CaO	1.14	1.32	1.31	1.47	1.14	1.35	1.73	2.13	1.77	1.91	1.93	1.48	1.48
Na_2O	3.70	4.91	4.87	4.52	4.95	4.52	4.79	5.8	6.48	5.86	5.06	4.93	4.63
K_2O	5.34	3.76	3.29	4.53	3.68	3.73	0.19	0.19	0.35	0.34	2.31	3.57	4.11
P_2O_5	0.01	0.01	0.05	0.06	0.05	0.04	0.08	0.06	0.07	0.08	0.11	0.05	0.08
Cr_2O_3	<0.01	<0.01	<0.01	<0.01	0.01	<0.01	<0.01	<0.01	<0.01	<0.01	0.01	<0.01	0.01
NiO	<0.01	<0.01	<0.01	<0.01	<0.01	<0.01	<0.01	<0.01	<0.01	<0.01	<0.01	<0.01	<0.01
LOI	0.52	<0.01	1.18	1.79	<0.01	<0.01	<0.01	<0.01	<0.01	<0.01	<0.01	<0.01	<0.01
TOTAL	**100.5**	**100.0**	**99.8**	**100.2**	**100.1**	**100.2**	**100.1**	**100.0**	**100.3**	**100.0**	**99.89**	**99.61**	**100.0**
Li (ppm)	<0.01	7.35	19.7	<0.01	18.7	12.2	22.7	42.6	27.3	22.8	6.33	9.25	14.3
P	10.1	34.6	225	216	198	163	316	245	294	309	421	229	354
Sc	0.20	0.32	1.55	0.82	1.85	0.91	1.97	1.58	2.56	2.09	1.61	1.56	1.48
Ti	215	266	878	865	1060	656	1200	1120	1090	1040	1920	1060	1585
V	3.32	13.5	13.5	12.7	10.4	10.1	10.1	122	9.17	11.4	26.5	30.1	26.4
Cr	6.98	2.54	21.4	12.5	4.29	3.55	5.68	5.32	5.68	4.91	4.69	5.72	5.25
Co	1.85	1.92	2.68	2.90	2.72	2.23	3.25	4.14	3.55	3.25	5.47	3.25	3.33
Ni	4.94	7.61	42.6	6.72	6.92	5.20	18.3	16.2	11.6	10	7.48	5.84	8.77
Cu	5.47	4.96	179	4.90	7.02	4.49	5.62	3.52	4.02	3.46	8.59	14.8	27.9
Zn	10.7	7.06	99.1	29.0	26.3	11.4	16.5	15.4	17.3	8.59	15.5	16.2	17.6
Ga	19.0	15.1	13.5	14.1	14.5	13.0	11.4	15.4	13.9	8.86	11.3	15.6	10.3
As	0.05	0.04	0.21	0.17	0.05	0.05	0.06	0.06	0.06	0.06	0.15	0.07	0.07
Rb	135	104	65.7	101	95.5	85.0	5.76	4.34	5.33	7.12	29.5	87.1	37.0
Sr	382	113	232	214	284	252	544	329	494	287	238	215	193
Y	0.14	0.39	1.56	2.41	2.01	3.64	3.48	1.56	3.61	4.37	5.17	2.67	3.97
Zr	5.26	15.7	94.1	81.8	73.6	67.2	79.1	85.2	81.0	103	139	91.2	120
Nb	0.74	0.42	2.03	3.74	4.74	2.77	4.54	4.69	4.79	3.9	5.43	3.75	5.53
Ba	914	456	1048	545	720	1020	32.2	32.7	59.4	85.9	407	625	494
Sn	<0.01	0.32	1.10	<0.01	0.84	0.74	0.77	0.75	0.84	0.69	0.99	0.65	0.92
Cs	1.35	1.27	2.66	3.40	2.95	2.24	1.68	0.68	1.45	0.78	2.01	1.79	1.62
La	1.01	1.40	5.98	14.4	11.2	5.82	13.6	10.6	14.2	17.2	21.2	12.9	14.3
Ce	1.13	1.34	9.85	29.1	17.6	8.80	28.6	26.4	27.4	20.7	25.3	26.4	18.2
Pr	0.10	0.16	1.32	2.94	2.31	1.28	2.89	2.01	2.97	3.60	4.54	3.16	3.24
Nd	0.32	0.56	4.48	10.1	7.68	4.67	9.66	6.62	10.2	11.9	15.2	10.9	11.0
Sm	0.70	0.35	1.15	1.82	1.50	1.47	1.47	0.92	1.58	1.91	2.51	1.93	1.95
Eu	0.60	0.56	0.56	0.64	0.69	0.83	0.33	0.31	0.40	0.52	0.72	0.89	0.75
Gd	0.04	0.08	0.64	1.36	0.91	0.73	1.36	0.91	1.41	1.55	1.82	1.34	1.36
Tb	<0.01	<0.01	0.07	0.13	0.09	0.09	0.14	0.07	0.15	0.18	0.21	0.13	0.15
Dy	0.02	0.06	0.29	0.50	0.41	0.57	0.69	0.32	0.72	0.85	1.01	0.55	0.73
Ho	<0.01	<0.01	0.05	0.07	0.06	0.10	0.11	0.03	0.10	0.13	0.16	0.08	0.12
Er	<0.01	0.03	0.16	0.19	0.19	0.29	0.30	0.14	0.29	0.37	0.47	0.22	0.32
Tm	<0.01	<0.01	0.02	0.02	0.02	0.04	0.03	0.01	0.03	0.04	0.06	0.02	0.04
Yb	0.01	0.04	0.17	0.18	0.17	0.30	0.23	0.11	0.23	0.31	0.41	0.16	0.25
Lu	<0.01	<0.01	0.03	0.03	0.02	0.04	0.03	0.01	0.03	0.04	0.06	0.02	0.03
Hf	0.21	0.47	2.76	2.55	2.15	2.28	2.12	2.37	2.27	2.90	3.75	2.60	3.42
Ta	0.04	0.03	0.11	0.09	0.18	0.26	0.14	0.17	0.12	0.20	0.53	0.15	0.25
W	0.01	0.08	0.11	0.17	0.10	0.07	0.13	0.21	0.16	0.11	0.17	0.09	0.13
Pb	7.08	5.76	40.1	10.2	12.1	15.5	4.26	4.49	6.58	5.58	5.71	9.82	5.20
Th	0.08	0.15	1.47	3.41	2.72	0.81	2.89	1.86	2.46	3.43	2.82	2.36	2.93
U	0.19	0.77	0.52	0.79	0.49	0.71	0.53	1.14	0.58	2.30	5.13	1.13	4.78

Lithology	Granodioritic gneiss					Monzonitic gneiss							
Sample #	M4 GG-9	M4 GG-11	M4 MG-2	M4 MG-3	M4 GG-16	M4 GG-1	M4 GG-5	M4 GG-10	M4 AM-2	M4 AM-1	M4 AM-3	M4 AM-4	M4 AM-5
SiO_2 *(wt %)*	75.3	74.6	74.4	73.3	73.2	59.6	58.2	63.0	63.2	59.3	59.6	63.5	61.5
TiO_2	0.15	0.19	0.20	0.19	0.16	0.97	0.99	0.70	0.74	0.87	0.90	0.73	0.81
Al_2O_3	14.2	14.6	14.5	14.6	14.9	18.3	18.4	17.8	17.4	18.1	18.88	17.3	18.3
FeO^{tot}	1.63	1.30	1.82	1.27	1.55	6.42	6.54	5.04	5.01	6.34	6.00	5.27	5.61
MnO	0.02	0.02	0.02	0.02	0.02	0.10	0.08	0.04	0.05	0.08	0.10	0.08	0.09
MgO	0.49	0.77	0.54	0.33	0.43	2.00	2.45	2.04	1.69	1.91	2.02	1.69	1.82
CaO	1.46	1.55	1.20	2.13	1.63	4.31	3.67	2.89	3.23	4.33	3.31	3.14	3.48
Na_2O	5.22	5.70	5.67	6.49	5.27	6.00	6.64	6.78	6.27	6.50	5.36	6.25	6.92
K_2O	1.69	1.33	1.96	1.48	2.82	2.02	2.25	1.61	2.20	2.09	3.48	1.70	1.47
P_2O_5	0.06	0.07	0.07	0.05	0.06	0.55	0.57	0.40	0.41	0.50	0.51	0.40	0.45

(*continued on next page*)

Table 1 (*continued*)

Lithology	Granodioritic gneiss					Monzonitic gneiss							
Sample #	M4 GG-9	M4 GG-11	M4 MG-2	M4 MG-3	M4 GG-16	M4 GG-1	M4 GG-5	M4 GG-10	M4 AM-2	M4 AM-1	M4 AM-3	M4 AM-4	M4 AM-5
Cr_2O_3	<0.01	<0.01	0.01	<0.01	<0.01	0.01	0.01	<0.01	<0.01	0.02	0.01	<0.01	<0.01
NiO	<0.01	<0.01	<0.01	<0.01	<0.01	<0.01	<0.01	<0.01	<0.01	<0.01	<0.01	<0.01	<0.01
LOI	1.83	<0.01	<0.01	<0.01	<0.01	2.36	1.78	<0.01	<0.01	1.79	2.80	<0.01	<0.01
TOTAL	**100.2**	**100.1**	**100.4**	**100.0**	**100.0**	**100.3**	**99.8**	**100.3**	**100.3**	**100.0**	**100.2**	**100.1**	**100.5**
Li *(ppm)*	<0.01	26.7	29.8	14.5	18.7	<0.01	<0.01	43.9	30.3	<0.01	73.4	42.0	53.7
P	220	300	340	225	259	1900	2120	1680	1820	1730	2590	1940	2150
Sc	0.57	1.27	2.29	0.96	1.54	12.6	6.22	10.6	6.38	5.00	4.83	3.26	6.27
Ti	806	1170	115-	1090	972	3600	5200	4090	3750	4380	5350	4370	4720
V	26.8	18.5	14.1	14.6	16.7	82.9	80.8	73.4	68.3	79.2	78.5	68.8	68.2
Cr	22.8	6.42	6.77	4.10	5.17	228	55.3	13.6	7.77	127	23.3	10.7	11.1
Co	2.45	4.34	3.46	2.79	3.39	8.85	13.8	19.7	7.68	11.0	14.7	11.4	11.4
Ni	6.76	7.39	6.85	5.75	5.88	17.9	15.5	14.0	13.1	14.6	42.6	11.8	11.3
Cu	8.30	8.19	3.93	4.87	6.17	8.77	21.0	26.5	10.2	49.2	137	22.6	9.78
Zn	12.2	21.1	14.4	41.4	26.1	49.8	65.9	23.2	26.3	42.3	130	51.6	62.4
Ga	15.0	16.2	15.1	15.5	18.0	14.0	20.8	18.4	14.8	21.0	26.4	25.0	29.5
As	0.14	0.06	0.07	0.05	0.07	0.85	0.73	0.25	0.27	0.68	0.57	0.22	0.26
Rb	41.3	13.6	62.7	37.4	79.8	72.6	65.4	20.5	34.4	20.4	70.0	14.4	39.4
Sr	361	175	427	368	708	453	801	588	577	629	539	728	906
Y	1.80	3.55	6.00	3.01	3.79	29.7	14.0	21.7	26.9	15.4	43.5	13.1	39.0
Zr	58.5	89.0	127	98.9	89.5	154	86.6	135	221	181	297	147	140
Nb	2.01	6.63	5.78	9.47	3.73	12.9	8.07	12.7	23.2	15.3	28.8	13.2	26.2
Ba	573	246	516	467	1130	247	661	325	370	280	744	241	256
Sn	<0.01	0.92	1.29	1.43	0.78	<0.01	<0.01	2.23	3.11	<0.01	4.66	2.89	4.10
Cs	4.14	0.97	2.73	4.15	2.27	3.71	22.9	2.37	3.73	4.39	5.80	3.72	4.20
La	9.95	12.71	11.1	9.16	16.0	59.0	70.8	62.5	67.8	65.2	54.4	55.2	79.4
Ce	21.0	27.6	20.5	24.0	26.1	98.0	157	116	76.3	131	108	99.9	151
Pr	1.83	2.70	2.53	1.78	2.90	14.1	14.7	13.5	14.0	12.0	15.1	10.7	17.6
Nd	5.94	9.18	9.14	6.06	9.25	49.0	49.1	47.4	47.5	39.0	55.0	36.8	60.0
Sm	1.21	1.45	2.02	1.11	1.85	8.26	7.54	7.55	7.49	5.86	11.4	5.05	10.5
Eu	0.51	0.43	0.65	0.49	0.87	1.59	2.00	1.56	1.57	1.48	1.90	1.20	1.75
Gd	0.81	1.26	1.54	0.88	1.13	7.71	7.19	7.08	6.37	5.78	10.6	4.77	9.68
Tb	0.07	0.13	0.19	0.07	0.11	1.03	0.71	0.88	0.83	0.59	1.56	0.51	1.31
Dy	0.32	0.66	1.09	0.43	0.60	5.43	3.04	4.40	4.39	2.76	8.70	2.42	7.13
Ho	0.05	0.11	0.19	0.06	0.10	0.97	0.48	0.75	0.79	0.48	1.58	0.41	1.27
Er	0.12	0.31	0.50	0.25	0.31	2.51	1.31	1.94	2.17	1.38	4.29	1.18	3.24
Tm	0.02	0.03	0.07	0.03	0.04	0.37	0.16	0.26	0.31	0.21	0.64	0.16	0.46
Yb	0.15	0.25	0.47	0.27	0.32	2.27	0.97	1.58	1.90	1.37	3.65	1.10	2.55
Lu	0.02	0.03	0.06	0.04	0.04	0.32	0.14	0.21	0.27	0.21	0.46	0.16	0.33
Hf	1.68	2.54	3.63	2.79	2.45	3.34	1.98	2.97	4.99	3.98	7.02	3.42	3.22
Ta	0.10	0.48	0.45	0.99	0.33	1.39	0.97	1.81	2.21	1.96	3.86	1.31	2.93
W	0.12	0.21	0.19	0.14	0.04	0.11	0.12	0.29	0.48	0.21	0.18	0.13	0.17
Pb	6.09	5.48	7.62	8.43	15.5	5.13	7.42	4.99	4.26	6.05	22.6	10.7	11.4
Th	1.60	1.96	2.43	3.65	2.90	6.40	4.02	6.89	10.1	5.77	6.98	5.64	12.7
U	0.66	0.97	1.30	4.12	1.87	1.94	1.76	2.68	6.02	3.49	1.92	2.07	2.17

Abbreviations: weight percent (wt%); and parts per million (ppm).
Detection limits for XRF analyses are 0.01% and ICP-MS are 0.01 ppm.

faults truncate, brecciate and displace quartz and feldspar grains containing shock microtextures (Gibson et al., 2024), and these grains also occur as clasts in the cataclasite fault fill and in the aphanitic dykes. The fault breccias, cataclasites and aphanitic dykes are, in turn, cut by hydrothermal veins, and their matrices are altered to low temperature (principally smectite-zeolite) assemblages that are related to the post-impact hydrothermal system (Wela, 2017).

A pervasive network of small-scale faults that show mm- to cm-scale displacements of the gneiss foliation, layering, pre-impact quartz veins and large crystals, affects all gneisses and dolerites (Fig. 4a and b). Fault spacing varies from a few dm to <1 cm. Faults intersect and mutually displace one another, with no consistent relative timing relationships, implying concomitant development. Individual faults range from planar to anastomosing and curved, with stepping between moderately dipping and steep segments being relatively common. Straight fault segments locally step along mm- to cm-scale sigmoidal to rhomb-shaped microbreccia lenses with the same overall monoclinic asymmetry (Fig. 4b). Apparent offset of features is most commonly reverse (hanging wall up), although slickenlines (Fig. 4c) in the fault gouge show variable pitch along the fault surfaces. Given their pervasive distribution and common association with sigmoidal cataclastic fabrics (Fig. 4b–d) we describe these faults as shear faults, following the proposal of Riller et al. (2018).

Intersecting shear faults create macroscopically visible brecciation of the wallrock (Fig. 5a and b). At their most intense, the shear faults in the gneisses merge and widen into cataclasite zones up to several centimetres wide (Fig. 5a). Cataclasite is best developed at 142–160 m and 263–292 m depths, near the main breccia dyke intersections (Fig. 2). Large lithic clasts within the clastic and aphanitic dykes show the same shear fault patterns as the wallrocks (Fig. 5b–d), and dyke apophyses exploit shear faults while intruding and isolating lithic clasts (Fig. 5b). Based on these patterns, we interpret the M4 drill core as comprising a highly faulted parautochthonous crater basement sequence disrupted by two Dm-wide fault zones and ubiquitous small-scale secondary faults that together accommodated horizontal shortening and vertical extension within the rock volume.

Table 2
Whole-rock compositions of the metadolerites and dolerites from the M4 drill core. Major elements by XRF analysis are provided in weight percent and trace elements by ICP-MS are provided in parts per million.

Lithology	Metadolerite			Silicified metadolerite		Dolerite		
Sample #	M4 A-1	M4 A-2	M4 A-3	M4 IS-2	M4 IS-1	M4 SILL-1	M4 B-1	M4 B-2
SiO_2 (wt%)	56.0	55.4	56.0	70.4	56.9	53.2	54.0	54.0
TiO_2	0.95	0.87	0.93	0.51	0.92	1.36	1.32	1.32
Al_2O_3	11.5	12.8	12.7	12.4	17.5	14.1	13.5	13.7
FeO^{tot}	10.1	10.4	9.84	4.84	7.25	13.5	13.0	12.5
MnO	0.18	0.14	0.11	0.03	0.08	0.19	0.19	0.18
MgO	8.70	8.26	8.08	1.36	0.44	5.68	5.58	5.53
CaO	9.96	9.80	12.2	9.26	14.5	8.68	7.10	7.78
Na_2O	2.12	1.87	0.69	1.10	1.50	2.92	3.94	3.39
K_2O	0.29	0.21	0.09	0.10	0.06	0.94	1.16	1.12
P_2O_5	0.14	0.13	0.14	0.13	0.52	0.14	0.13	0.14
Cr_2O_3	0.09	0.07	0.07	0.02	0.01	0.02	0.02	0.02
NiO	0.04	0.03	0.03	<0.01	<0.01	0.01	0.01	0.01
LOI	2.46	<0.01	<0.01	<0.01	2.33	2.21	3.47	4.32
TOTAL	**100.1**	**99.98**	**100.9**	**100.2**	**99.68**	**100.7**	**99.95**	**99.69**
Li (ppm)	<0.01	46.9	55.1	11.3	<0.01	<0.01	<0.01	67.6
P	484	534	591	552	2000	593	491	778
Sc	29.7	40.4	43.1	17.9	5.33	24.6	26.5	20.7
Ti	2790	4960	5370	2870	5290	3980	7580	8480
V	221	216	213	95.2	118	269	265	315
Cr	420	494	510	204	35.4	44.4	71.4	64.2
Co	23.4	57.2	44.5	7.40	8.48	28.6	55.0	55.2
Ni	115	193	197	27.6	16.3	44.7	71.8	107
Cu	29.8	46.4	44.3	3.83	5.91	63.3	134	143
Zn	36.5	63.3	41.4	27.9	20.5	69.5	214	101
Ga	8.75	16.1	17.0	20.0	32.9	11.2	18.6	18.7
As	0.78	0.55	0.52	0.42	1.57	1.04	0.96	0.35
Rb	6.07	9.07	4.27	7.47	4.52	31.0	68.3	70.0
Sr	358	594	880	1230	1600	227	339	465
Y	16.0	21.9	22.7	13.2	19.1	20.3	20.2	20.7
Zr	56.7	80.4	77.5	72.1	101	55.0	102	108
Nb	2.40	4.25	4.45	5.28	9.19	3.76	5.58	5.86
Ba	43.6	61.9	14.2	33.4	9.19	116	204	361
Sn	<0.01	1.01	1.01	1.31	<0.01	<0.01	<0.01	1.63
Cs	0.83	0.92	0.55	20.0	12.5	3.10	4.88	7.06
La	11.7	18.6	19.8	23.9	88.5	13.4	13.6	12.3
Ce	20.9	29.0	30.8	35.9	171	20.6	29.5	25.4
Pr	3.29	4.63	4.99	5.00	18.0	3.82	3.82	3.49
Nd	13.5	18.5	19.8	17.4	57.5	15.8	15.7	14.6
Sm	2.77	3.81	4.03	3.08	8.22	3.46	3.56	3.74
Eu	0.81	1.07	1.10	1.04	2.13	0.99	1.02	1.20
Gd	2.81	3.75	4.06	3.00	8.45	3.46	3.67	4.05
Tb	0.46	0.60	0.64	0.41	0.91	0.58	0.60	0.65
Dy	2.80	3.72	3.97	2.24	3.97	3.60	3.72	3.91
Ho	0.57	0.73	0.80	0.42	0.63	0.73	0.75	0.78
Er	1.45	1.96	2.05	1.11	1.54	1.83	1.88	2.09
Tm	0.22	0.29	0.30	0.15	0.20	0.28	0.27	0.32
Yb	1.34	1.73	1.83	0.96	1.18	1.65	1.73	1.97
Lu	0.20	0.25	0.26	0.14	0.17	0.25	0.26	0.30
Hf	1.42	1.97	1.92	1.87	2.16	1.41	2.68	2.97
Ta	0.13	0.23	0.25	0.33	0.45	0.22	0.35	0.37
W	0.61	0.30	0.59	0.31	0.36	0.28	0.35	0.48
Pb	1.04	1.93	2.03	1.73	3.50	3.80	8.45	10.5
Th	0.92	1.32	1.41	2.97	4.36	2.08	2.18	1.94
U	0.24	0.26	0.26	1.77	5.27	0.30	0.56	0.60

Abbreviations: weight percent (wt%); and parts per million (ppm).
Detection limits for XRF analyses are 0.01% and ICP-MS are 0.01 ppm.

5.2. Microscopic features

The shear faults in the granitoids are marked by microbrecciation and cataclasis of mineral grains. Individual microcataclastic to ultracataclastic zones in the granitoid gneisses range from a few tens of μm to >1 mm wide but locally merge into mm- to cm-wide zones with a heterogeneous planar to monoclinic-sigmoidal internal fabric (Fig. 4b–d). The cataclasite comprises angular to subrounded and variably comminuted mineral clasts of quartz, feldspar, biotite, titanite, epidote, and/or (titano)magnetite in a microcrystalline matrix displaying cataclastic flow that is corroded and cemented by hydrothermal zeolites ± smectites. The quartz fragments may display decorated PDF with varying amounts of rotation between adjacent fragments, but curved PDF are also common and can be correlated with intracrystalline strain evidenced by undulose extinction, deformation bands and tiltwalls (Gibson et al., 2024). The preferential localisation of these internal strain features in the vicinity of the shear faults confirms their link to the latter and, thus, the post-shock timing of the faults. Microscale oblique sigmoidal fabric elements showing the same sense of asymmetry as their macroscopic counterparts were formed by differential shear of cataclastic aggregates derived from the coarse-grained granitoid precursor mineral assemblage (Fig. 4d).

Table 3
Whole-rock compositions of the aphanitic dykes from the M4 drill core. Major elements by XRF analysis are provided in weight percent and trace elements by ICP-MS are provided in parts per million.

Lithology	Aphanitic dykes							
Sample #	M4 IM1	M4 IM3	M4 IM4	M4 IM5	M4 IM6	M4 IM7	M4 IM8	RG M4-LL-01
SiO_2 (wt%)	61.0	62.5	58.9	64.1	63.3	59.4	61.5	61.3
TiO_2	0.96	0.77	0.89	0.65	0.78	0.99	0.95	0.60
Al_2O_3	14.1	14.8	15.7	15.5	15.1	15.0	14.6	12.7
FeO^{tot}	9.26	7.29	7.82	5.26	6.51	8.72	7.86	5.12
MnO	0.10	0.10	0.10	0.07	0.09	0.13	0.10	0.06
MgO	8.46	4.59	4.57	2.58	3.74	3.67	3.32	4.00
CaO	4.95	5.26	6.28	4.29	4.68	5.20	4.33	4.29
Na_2O	1.01	3.89	4.18	4.73	3.84	4.64	5.39	4.79
K_2O	0.23	1.80	1.55	3.09	2.35	1.98	1.83	0.26
P_2O_5	0.11	0.21	0.24	0.28	0.26	0.24	0.25	0.16
Cr_2O_3	0.07	0.03	0.02	0.01	0.02	0.01	0.01	0.02
NiO	0.02	0.01	0.01	0.01	0.01	0.01	0.01	0.01
LOI	<0.01	4.60	3.78	3.27	4.29	4.57	4.70	6.23
TOTAL	**100.3**	**101.3**	**100.3**	**100.6**	**100.7**	**99.99**	**100.2**	**99.54**
Li (ppm)	106	80.9	38.7	44.5	67.9	40.5	26.9	78.4
P	423	882	1090	1170	1360	1270	1130	624
Sc	40.1	7.99	6.62	5.58	7.15	6.64	4.88	11.3
Ti	3890	4120	4860	3870	4640	6280	4870	3100
V	162	120	150	90.1	130	195	143	77.6
Cr	312	166	119	65.3	150	55.3	50.5	109
Co	16.1	25.5	28.3	18.8	22.5	36.1	22.1	14.3
Ni	90.6	101	102	59.3	90.7	84.6	62.6	63.9
Cu	7.58	36.0	74.1	40.7	69.5	90.9	65.4	8.49
Zn	40.8	57.9	57.5	60.3	116	75.0	63.4	35.7
Ga	15.3	19.3	19.4	16.5	19.9	17.2	18.4	21.9
As	0.49	0.37	0.74	0.54	0.29	0.32	0.34	<0.01
Rb	8.85	64.7	58.3	57.4	81.5	98.1	50.7	13.3
Sr	525	507	516	778	587	599	236	399
Y	21.5	16.3	17.9	12.2	16.7	22.2	16.0	10.3
Zr	91.5	130	142	133	144	138	127	65.9
Nb	4.92	9.32	9.78	13.0	9.74	11.7	11.0	6.33
Ba	25.5	476	478	921	671	722	582	79.8
Sn	0.82	1.25	0.84	1.11	1.19	1.66	1.33	1.83
Cs	2.91	2.57	1.85	2.09	2.19	3.08	1.31	2.18
La	21.3	27.1	27.4	27.0	27.7	29.2	27.2	24.9
Ce	23.8	58.2	58.3	58.1	56.0	57.4	51.7	49.6
Pr	4.93	6.86	6.99	6.99	6.97	6.96	6.11	5.40
Nd	18.0	26.3	26.3	25.4	26.1	26.0	22.9	20.6
Sm	3.58	4.89	5.20	4.92	5.13	5.48	4.45	3.77
Eu	1.13	1.44	1.46	1.45	1.47	1.49	1.21	1.13
Gd	3.60	4.58	4.97	4.41	4.78	5.49	4.37	3.34
Tb	0.59	0.60	0.67	0.54	0.63	0.78	0.58	0.43
Dy	3.72	3.12	3.58	2.66	3.24	4.31	3.11	2.32
Ho	0.76	0.58	0.67	0.48	0.60	0.82	0.59	0.44
Er	1.98	1.56	1.82	1.31	1.62	2.17	1.60	1.15
Tm	0.29	0.23	0.26	0.19	0.24	0.33	0.24	0.15
Yb	1.82	1.40	1.62	1.15	1.46	1.99	1.44	1.02
Lu	0.27	0.21	0.24	0.17	0.22	0.29	0.22	0.14
Hf	2.31	3.33	3.67	3.37	3.62	3.59	3.28	1.80
Ta	0.26	0.64	0.68	0.86	0.85	1.18	0.91	0.47
W	0.92	0.55	0.42	0.40	0.48	0.53	0.39	0.41
Pb	2.41	15.1	11.0	11.6	11.6	10.3	9.06	7.67
Th	2.66	3.52	3.74	3.25	3.78	4.16	3.58	3.67
U	1.86	1.80	1.79	2.16	1.89	1.50	1.58	1.52

Lithology	Aphanitic dykes					
Sample #	RG M4-LL-02	RG M4-LL-03	M4 IM2	RG M4-LL-04	RG M4-LL-05	RG M4-LL-06
SiO_2 (wt%)	60.6	64.4	71.8	71.1	71.9	70.5
TiO_2	0.74	0.51	0.25	0.28	0.24	0.26
Al_2O_3	14.5	15.1	14.9	13.7	13.4	13.4
FeO^{tot}	6.89	3.52	2.04	1.41	1.77	2.25
MnO	0.08	0.04	0.02	<0.01	0.02	0.01
MgO	3.49	2.00	1.01	1.76	1.16	1.06
CaO	5.14	4.48	4.37	2.28	3.02	3.23
Na_2O	5.02	5.33	5.40	5.05	4.80	5.15
K_2O	0.80	0.43	0.25	0.12	0.14	0.12
P_2O_5	0.18	0.24	0.14	0.09	0.11	0.12
Cr_2O_3	0.02	0.01	0.01	0.01	0.01	<0.01

(*continued on next page*)

Table 3 (*continued*)

Lithology	Aphanitic dykes					
Sample #	RG M4-LL-02	RG M4-LL-03	M4 IM2	RG M4-LL-04	RG M4-LL-05	RG M4-LL-06
NiO	0.01	0.01	<0.01	<0.01	<0.01	<0.01
LOI	2.56	4.34	4.89	4.47	3.93	3.93
TOTAL	**100.0**	**100.4**	**100.2**	**100.3**	**100.5**	**100.0**
Li (ppm)	30.1	44.4	28.7	68.8	42.4	47.0
P	712	947	572	315	411	474
Sc	14.2	5.84	1.13	2.00	2.19	2.35
Ti	3940	2650	1310	1380	1230	1320
V	101	44.8	32.4	14.3	11.9	24.2
Cr	129	47.1	15.9	4.68	4.33	4.57
Co	20.8	8.61	4.14	3.63	3.89	2.84
Ni	70.9	38.9	30.5	6.67	8.04	6.00
Cu	17.9	3.96	16.2	1.63	2.91	2.82
Zn	35.0	35.9	30.7	17.7	19.9	11.8
Ga	20.6	17.3	12.9	18.2	14.8	16.9
As	<0.01	<0.01	0.43	<0.01	<0.01	<0.01
Rb	36.2	21.3	8.17	3.85	7.81	6.36
Sr	452	584	629	311	485	516
Y	11.9	10.4	6.86	2.94	3.88	4.91
Zr	65.7	43.1	111	30.1	46.0	37.2
Nb	6.91	8.42	5.33	4.27	4.21	4.90
Ba	250	158	100	32.9	86.0	38.3
Sn	1.96	2.36	0.98	1.33	1.50	1.97
Cs	0.78	2.50	3.07	0.62	2.09	1.94
La	28.5	34.6	18.9	15.9	18.4	26.1
Ce	55.0	64.6	37.4	27.7	35.9	49.7
Pr	5.93	6.92	4.11	3.19	3.60	5.01
Nd	22.5	25.2	14.6	11.1	13.0	17.5
Sm	4.10	4.47	2.48	1.81	2.20	2.84
Eu	1.25	0.98	0.63	0.61	0.74	0.88
Gd	3.69	3.85	2.44	1.38	1.73	2.25
Tb	0.48	0.47	0.30	0.15	0.20	0.25
Dy	2.69	2.38	1.41	0.72	0.94	1.20
Ho	0.50	0.42	0.24	0.12	0.16	0.20
Er	1.35	1.05	0.65	0.31	0.39	0.50
Tm	0.18	0.13	0.09	0.04	0.05	0.06
Yb	1.20	0.86	0.56	0.25	0.33	0.39
Lu	0.17	0.11	0.08	0.04	0.05	0.05
Hf	1.81	1.20	2.90	0.91	1.30	1.02
Ta	0.50	0.52	0.33	0.25	0.31	0.36
W	0.52	0.32	0.27	0.24	0.18	0.22
Pb	10.2	5.57	2.93	5.09	8.14	4.54
Th	3.92	4.33	2.93	2.87	2.54	3.21
U	2.55	2.54	2.00	1.06	1.50	2.32

Abbreviations: weight percent (wt%); and parts per million (ppm).
Detection limits for XRF analyses are 0.01% and ICP-MS are 0.01 ppm.
Abbreviations: weight percent (wt%); and parts per million (ppm).
Detection limits for XRF and ICP-MS analyses are 0.01% and 0.01 ppm respectively.

The high levels of oxidation and smectite alteration limit microtextural analysis of the faults and cataclasites in the doleritic rocks. However, dolerite clasts in the dykes are disaggregated to varying degrees, suggesting that similar cataclastic processes affected the mafic rocks.

6. Aphanitic breccia dykes

The widespread post-impact hydrothermal alteration in the M4 drill core means that no evidence remains of either glass or melt crystallisation textures in the aphanitic dykes. Nonetheless, as explained below, a melt origin is deduced from a combination of evidence of intrusive geometries and flow banding that suggest a low-viscosity phase capable of significant flow (Figs. 3–8), and that retains a distinctly different texture to that of the cataclasite, notwithstanding the comprehensive hydrothermal overprint (Fig. 6). No petrographic or XRD evidence was found of high-pressure silica or feldspar polymorphs or glasses within or associated with the dykes and faults (Wela, 2017).

6.1. Macroscopic features

Individual aphanitic dykes in the M4 drill core range in width up to ~2 m (Fig. 2) and may be as thin as a few millimetres. The comprehensive hydrothermal overprint makes it difficult to unequivocally confirm if some thinner features are also dykes; however, discontinuous lenses as small as a few mm in length and <1 mm wide that occur along shear faults show internal evidence of flow folding and clasts (Fig. 8a), and an identical hydrothermal paragenesis and matrix texture to the larger dykes. Most of the dykes – and all the most voluminous dykes – are red to reddish brown. Small pink or orange dykes (Figs. 3 and 4e) are only found in the granitoid rocks, and thin grey dykes (Fig. 4a) are only found in the silicified metadolerite; however, the red and red-brown dykes (Figs. 3, 5 and 7) occur in both the doleritic and granitoid rocks, although the latter always lie close to doleritic rock intersections. Dyke matrices range from homogeneous to variegated (Fig. 7), with colour change ranging from sharp to gradational. While some dyke margins display a distinct colour change relative to the dyke interior, the pervasive hydrothermal alteration precludes conclusive identification of chill margins. Similarly, no consistent variations in clast size or clast:

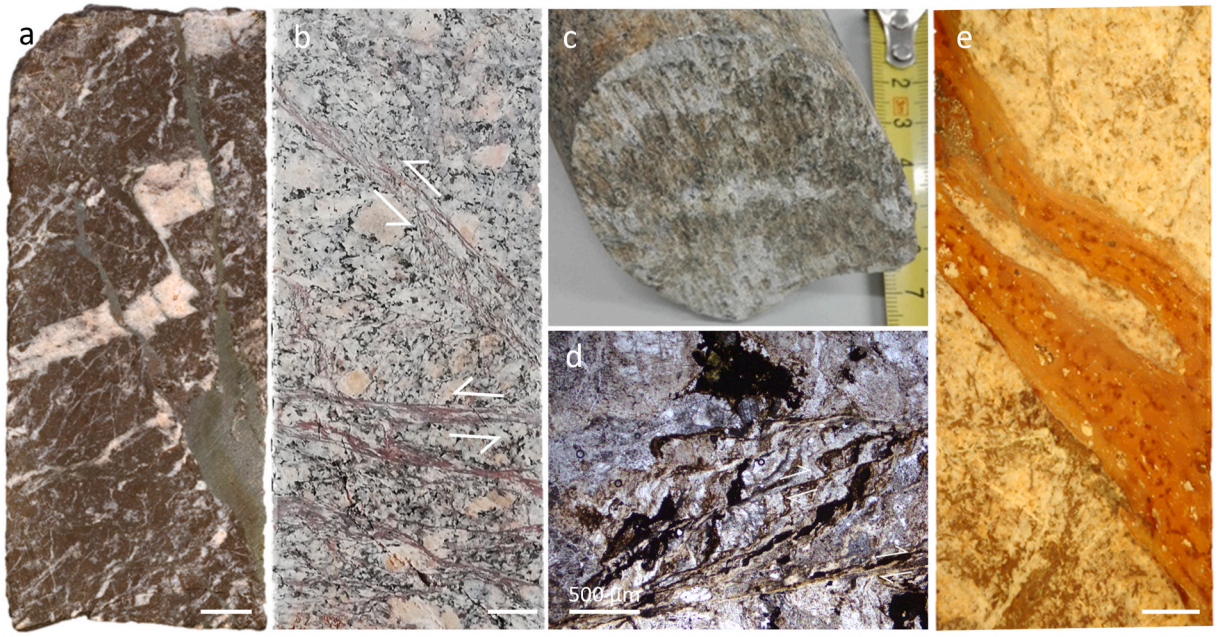


Fig. 4. Impact-related structural and dyke features of the M4 drill core. (a) Silicified metadolerite from 206.3 m depth, showing pre-impact quartz veins displaced by impact-related shear faults that are intruded by a branching grey aphanitic breccia dyke. (b) Granitoid gneiss from 131.0 m depth showing shear faults with monoclinic asymmetry consistent with reverse slip displacement. (c) Shear fault surface showing slickenlines, from 362.1 m depth. (d) Photomicrograph showing microscopic character of shear faults in granitoid gneiss from 131.0 m depth (cataclastic flow with reverse slip sense). Field of view 3 mm across. (e) Orange aphanitic breccia dyke in granitoid gneiss from 230.1 m depth. The dyke shows flow lamination and alignment of an elongate, slightly boudinaged, clast of cataclased gneiss, as well as smaller mineral clasts. Scale bars correspond to 1 cm.

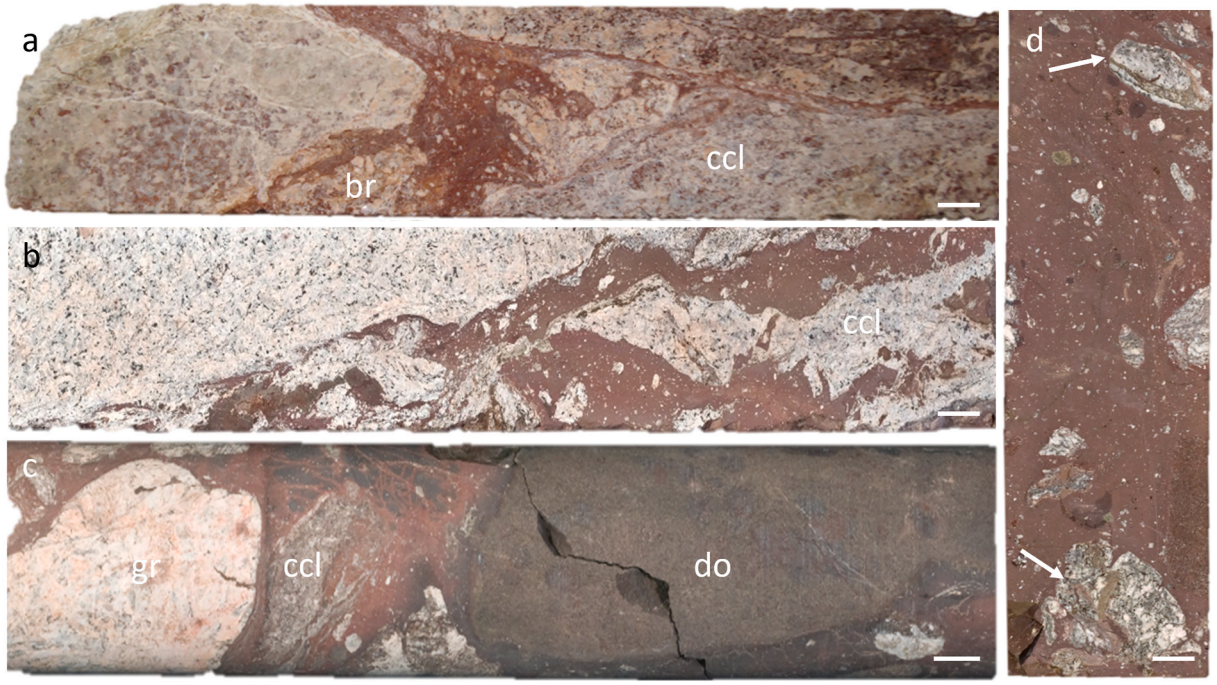


Fig. 5. Red aphanitic breccia dyke features in the M4 drill core. (a) Clast-rich aphanitic dyke in cataclasite in granitoid gneiss, from 158.1 m depth. Note the cuspate-lobate contacts and the extreme length of the dyke apophyses in the upper part of image. (b) Dyke intruding granitoid gneiss with stepped contact and rhomb-shaped lithic clasts that suggest dilation along intersecting shear faults. Cataclasite mantles the lithic clasts and occurs along the dyke margins as elongate, boudinaged, masses and web-like stringers. From 296.0 m depth. (c) Polymictic aphanitic dyke containing dm-scale granite and dolerite clasts and an elliptical cataclasite mass (centre). Note the thin apophyses of dyke intruding the granite clast. From 260.4 m depth. (d) Aphanitic dyke containing lithic clasts of granitoid gneiss that contain smaller orange-red aphanitic dykes (arrows). From 259.1 m depth. Scale bars are 1 cm.

matrix proportions towards dyke margins could be discerned.

As mentioned previously, the small diameter of the M4 core severely limits investigation of the large-scale dyke geometry and nature of the dyke contacts. The most voluminous intersections cluster between 259 m and 296 m depth where their cumulative thickness (~13 m) approaches 35% of the core, with six intersections of >1 m (Fig. 2). These

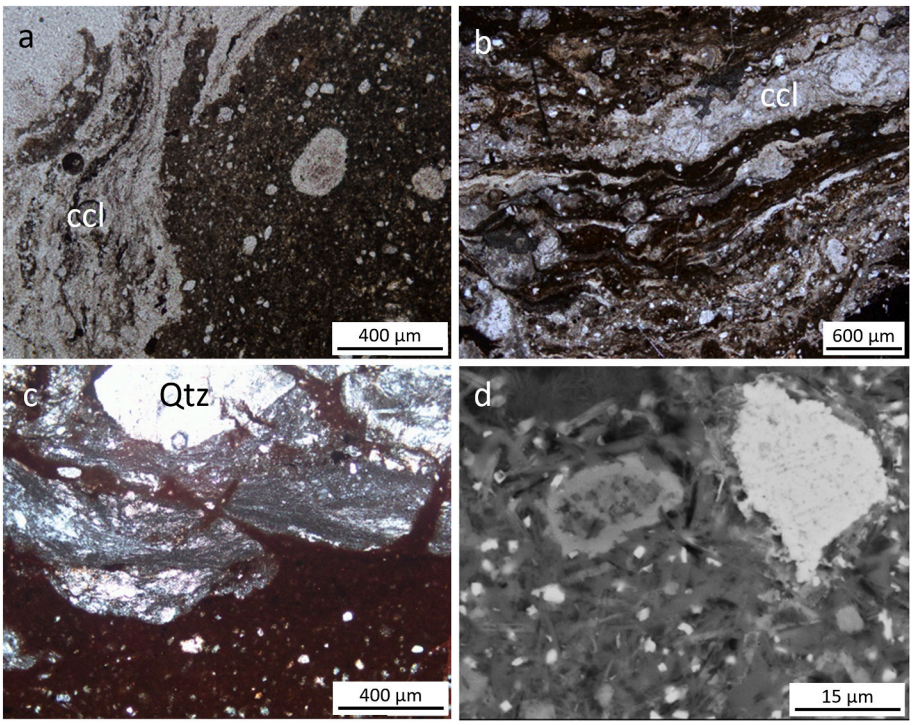


Fig. 6. Photomicrographs of aphanitic breccia dykes from the M4 drill core. (a) Infolding of aphanitic dyke (right) with cataclasite (left), from 271.2 m depth. Plane-polarised light (PPL). (b) Aphanitic dyke sample from 234.0 m depth displaying a schlieric-banded texture with cataclased quartz and feldspar occurring as boudinaged light bands and lenses in the darker dyke matrix. PPL. (c) Quartz clast with cataclased and partially dynamically recrystallized margin intruded by wedge-shaped aphanitic dyke apophyses; sample from 259.1 m depth. Crossed polarised light (XPL). (d) BSEM image of aphanitic dyke matrix from 259.1 m depth showing recrystallization to hydrothermal smectites. Zeolite (light grey) occurs at bottom, left and rimming feldspar clast; subidioblastic fine-grained magnetite (white) occurs disseminated in the matrix and overgrowing the titanomagnetite clast.

intersections alternate with granite gneiss and dolerite that individually reach 2 m in width, and with cataclasite and clastic-matrix breccias (Fig. 3). The limited core diameter makes it impossible to tell if these intersections represent a single sheet-like dyke enclosing large lithic clasts, a more localised reservoir of network breccia with large clasts, or a series of discrete dykes in largely intact wallrock. Outside of this interval, individual dykes seldom exceed 10 cm width but are present at multiple depths throughout the core (Fig. 2). Given their smaller volumes relative to the core, these thin dykes provide more geometric information. Several display overall geometries typically described for pseudotachylite friction melts in fault zones (e.g., Sibson, 1975), comprising a generation plane within the shear fault and short wedge-shaped apophyses intruding into the adjacent wallrock (Fig. 8b). Thin dykes with orientations aligned close to the core axis show high aspect ratios ($\gg$10:1), and cuspate dyke terminations, consistent with a low-viscosity melt (Fig. 5a).

The dykes are characterised by an aphanitic matrix that is either homogeneous or finely laminated, which distinguishes them from the coarser-grained, mineralogically and texturally more diverse, cataclasite (Fig. 6a, b and d). The laminations may be planar and oriented approximately parallel to the dyke walls where the latter are planar but are locally folded into either asymmetric shear folds or, locally, more chaotic patterns and/or sheath fold geometries in dyke centres or adjacent to large clasts (Fig. 7). Dyke margins against the granitoid gneisses and dolerites are generally sharp but, in many cases, the dykes are flanked by, and variously intermingled with, cataclasite (Figs. 5a and b, 6a, b, and 7). Smaller dykes show evidence of finger-like intrusion into cataclasite zones, but others display evidence of disharmonic cuspate-lobate infolding of cataclasite along dyke margins (Figs. 5a and 6a). A distinctive feature of the dykes is that they contain irregular to planar and/or tight to isoclinally folded, highly attenuated and boudinaged, greyish white cataclasite masses, lenses and stringers that range from <1 mm to 10 cm wide (Figs. 3 and 5b–d). These can contain clasts up to several mm in size but their typical grain size is $\ll$1 mm (refer to Section 6.2). In places, the ratio of melt matrix to cataclasite approaches 1:1 (Fig. 6b), suggesting that a complete spectrum exists between the aphanitic dykes and cataclasite. Taken together, these features suggest that the cataclasite was incohesive at the time of dyke intrusion, supporting penecontemporaneous development of the two (see Discussion).

Macroscopically visible clasts constitute up to 30% of the volume of individual dykes but clast content may be as low as <5%. Generally, clast distribution in individual dykes is highly variable. Lithic clasts up to dm size vary from angular to subrounded and comprise primarily granitoid gneiss, but with dolerite and metadolerite also occurring in the larger dykes (Figs. 3 and 5b–d). The clast population in smaller dykes is more likely to be monomictic than that in the wider dyke intersections, which are generally polymictic.

The straight edges of angular lithic clasts are commonly parallel to internal shear faults within the clast, suggesting that large clasts were isolated within the dykes either by emplacement of the dykes along shear faults, or that the precursor melt was initially generated along these faults (Fig. 5a and b). The latter is supported by the presence of mm-thick aphanitic lenses and dykelets along the internal shear faults within some large clasts, similar to the feature seen in Fig. 8a; other clasts show wedge-shaped intrusive apophyses from the enclosing dyke (Fig. 5c and d). In places the planar clast edges still align with fractures in the wallrock adjacent to the dyke, and correlate spatially with stepped dyke margins, suggesting relatively passive dyke emplacement into a dilating en-echelon fracture array (Fig. 5b).

Lithic clasts locally display cataclasite mantles that trail off into the dyke matrix parallel to the flow lamination (Fig. 5b), confirming that large clasts became isolated by intrusion of dyke material along cataclasite-filled shear faults. In some cases, the lack of discernible

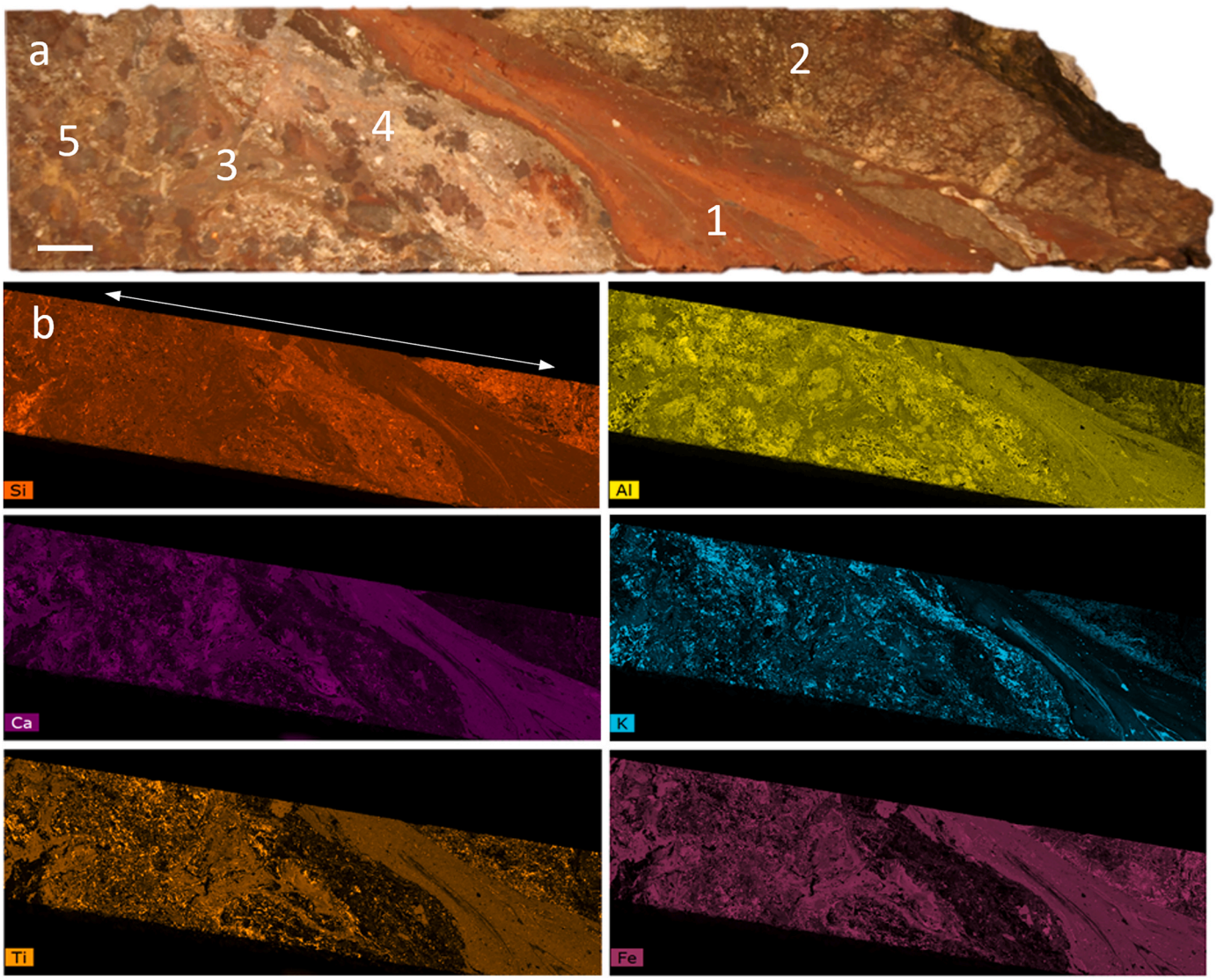


Fig. 7. Variegated red aphanitic breccia dyke from 264 m depth in a half-core section from the M4 drill core (a) and corresponding μXRF elemental distribution maps (b). The flow-laminated dyke (1) separates brecciated and cataclased dolerite (2) from a mixed granite-dolerite cataclasite (4) containing an irregular chaotically folded aphanitic mass (3), with cataclasite-rich aphanitic dyke (5) on the left. Elemental distribution patterns for Si, Al, Ca, K, Ti and Fe are explained in the text; brighter colour intensities correspond to higher X-ray counts. Double-sided arrow in Ti map corresponds to length of specimen in (a). Scale bar is 1 cm.

rotation of these clasts suggests a relatively passive intrusive mechanism. The incorporation of masses and stringers of cataclasite, and their subsequent flow-assisted disaggregation (Fig. 6a and b), provides an explanation for the irregular spatial distribution of clasts in the dykes and the lack of any consistent variation in clast size across individual dykes.

The dyke features described above mostly relate to dykes hosted in granitoid gneiss, owing to the strong colour, grain size and mineralogical contrasts with the wallrocks. The aphanitic dykes are less visible in the doleritic rocks owing to their mafic appearance and the hydrothermal alteration and oxidation overprints, which reduce the contrast between the dykes and their clasts and wallrocks. Nonetheless, similar mm-wide lenticular to planar bodies confined to shear faults, and more irregular clast-rich bodies up to several cm in size, are identifiable on cut surfaces of the core.

6.2. Microscopic features

Transmitted light petrographic analysis of the red to red-brown, black and grey dykes shows that the matrix is largely opaque in plane-polarised light and varies from black to brown and red-brown (Figs. 6a–c and 8a). It appears largely isotropic under crossed polarisers but analysis of the edges of thin sections shows that it is cryptocrystalline, rather than vitric. This is confirmed by BSEM, which shows a typically 1–10 μm grain size (Fig. 6d). Mineral chemistry and XRD (Wela, 2017; T. Masiu, pers. comm. 2023) confirmed the matrix typically comprises smectite, with subsidiary zeolite and magnetite, but garnet neoblasts have also been identified in a single small fault-hosted, flow-folded, lens in a sample from 346.0 m depth. Pink and orange dyke matrices typically show a mixed smectite-zeolite alteration paragenesis with a slightly coarser grain size of up to 50–100 μm. Locally the smectites are arranged in a spherulitic texture, with spherulites up to a few tens of microns across. The distribution of phases in the matrix appears to be relatively uniform within individual compositional laminae, suggesting that hydrothermal recrystallization occurred from a uniform precursor, which would be consistent with a glass or cryptocrystalline melt rock. BSEM imagery shows the homogeneous texture of the dyke matrix, with scattered small (<50 μm), angular to rounded mineral clasts, which contrasts with that of the cataclasite, which is composed primarily of coarser, angular clasts with a larger range of

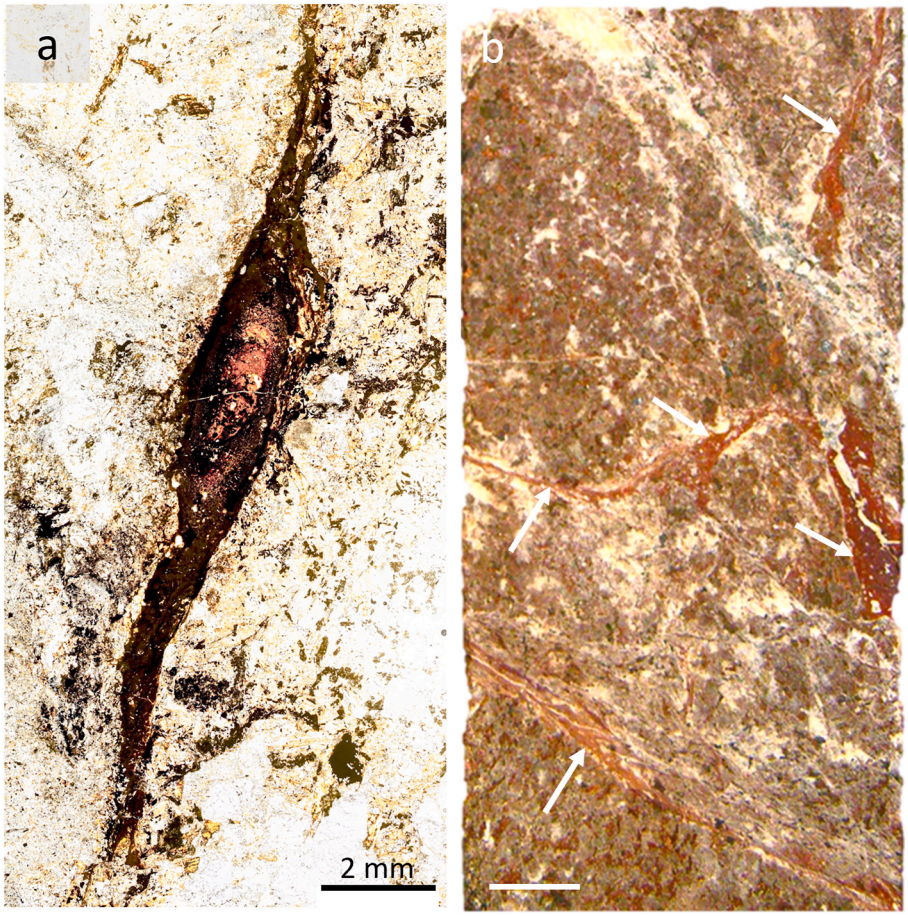


Fig. 8. Structural relationships of aphanitic breccia dykes and shear faults in the M4 drill core. (a) Thin section PPL image of granitoid gneiss from 346.0 m depth showing an aphanitic breccia lens containing sheath-like flow folding. (b) Faulted and hydrothermally altered granite gneiss from 146 m depth showing aphanitic dykes along shear faults (upward-pointing arrows) and in wedge-shaped apophyses off shear faults (downward-pointing arrows), consistent with the geometry of pseudotachylite found in tectonic faults. The white fracture fill is hydrothermal calcite + zeolite veining.

grain size (tens of μm up to mm; Fig. 6a and b). The much smaller grain size – by 1–2 orders of magnitude – of the hydrothermal minerals in the dyke matrices relative to the cataclasites is consistent with an originally glassy or ultra-fine-grained matrix lacking significant porosity for large hydrothermal mineral grains to grow, in contrast to the cataclasite.

Optically identifiable mineral clasts in the aphanitic dykes are dominated by rounded to angular quartz and microcline, with plagioclase being slightly less common. These clasts can reach several mm in size and are predominantly monomineralic, although some are polycrystalline, and mm-sized polymineralic clasts are also present. Clast minerals display the same range of internal strain features that are associated with the shear faults and their cataclasite fill and can display mantles (Fig. 6c) and/or tails of comminuted fragments that are streaked out into the matrix and help define the flow lamination (Fig. 6b). More rarely, monomineralic clasts of biotite, (titano)magnetite, epidote, titanite, zircon, and apatite are present. Apart from rare pyroxene, no unequivocally metadolerite- or dolerite-derived minerals have been identified, although plagioclase, magnetite and titanite could be derived from either a granitoid or a doleritic source. The mineral clast population thus appears strongly biased towards the granitoid rocks, in contrast to the more mafic character of the red dyke matrices (see Geochemistry); however, the lack of contrast between the dykes and the highly altered cataclased dolerite may have resulted in selection bias in sampling for petrography.

Fig. 6c shows a highly strained quartz clast displaying a cataclastic to dynamically recrystallized mantle. When combined with the macroscopic evidence of infolding and mingling of melt with cataclasite, the optical and electron microscopy together with μXRF, support an origin for much of the mineral clast fraction by mingling and partial assimilation of quartzofeldspathic cataclasite derived from shear faulting in the granitoid gneisses.

Several dykes contain small, mm-sized, rounded to elliptical vugs infilled by relatively coarse-grained hydrothermal minerals (zeolite, smectite, calcite, alkali feldspar, and/or magnetite-haematite) that are otherwise only found in cross-cutting hydrothermal veins. Given their size, we are not convinced that they represent original amygdules, however, this possibility cannot be completely dismissed.

7. Geochemistry

In the preceding section, structural evidence was presented that suggests that the mm- to cm-scale aphanitic dykes in the M4 drill core show multiple characteristics consistent with faulting-induced friction melt (i.e., pseudotachylite). However, the core also contains multiple voluminous, dm- to m-wide, dyke intersections where, notwithstanding the intimate relationship with cataclasite that supports a fault linkage, the alternative possibility needs to be considered that these could represent injections of impact melt along faults (e.g., Thompson and Spray, 2017). To investigate this, whole-rock major, trace and rare-earth element data were obtained for 14 dykes with individual widths exceeding 5 cm. Wherever possible, samples with large lithic clasts, cataclasite masses or cross-cutting hydrothermal veins were avoided to obtain the most representative compositions for the dyke matrix; however, given the macroscopic and microscopic evidence for significant

mechanical mingling and assimilation of cataclasite, and thin hydrothermal veins, at least some contamination is unavoidable.

7.1. Major element μXRF analysis

The issue of internal compositional heterogeneity was explored via μXRF scanning of one half-core sample section of an aphanitic dyke from a depth of 264 m. Selected μXRF element maps are shown in Fig. 7. This sample is representative of the interval hosting the most voluminous dyke breccia intersections in the core (Fig. 2). On the right of the sample the dyke (1) is bright red to red-brown, relatively clast-poor and displays strongly planar flow lamination against a largely coherent brecciated dolerite clast (2), whereas in the centre and towards the left (3) aphanitic dyke material displays an internal structure that is more chaotic, variegated and clast-rich (see Fe and Ti maps, Fig. 7b) where it is associated with partially disaggregated, cataclastic, granitoid- and dolerite-derived clasts (4, 5). The maps show that the clast-poor aphanitic dyke matrix is relatively enriched in Ca, Ti, and Fe and depleted in Si, K, and Al; however, in its centre it preserves an isoclinally folded layer and clasts that scanning confirms are enriched in Al, Si, and K, and depleted in Fe, Mg, and Ti (Fig. 7b). This supports derivation of the aphanitic dyke matrix primarily from a mafic source, but with mechanical mixing in of a clastic felsic component.

7.2. Major elements

Bulk rock compositional data for the lithologies in the M4 drill core are presented in Tables 1–3 The plots of major elements against SiO_2 for the various M4 drill core lithologies (Fig. 9) show that the host rocks form three broad clusters; however, some oxides show sufficient differences between the dolerite and metadolerite samples (Fig. 9b–e, f, and g) to suggest that these represent distinct end-member compositions. Gibson et al. (2022) discussed the distinctly more fractionated character of the monzonitic gneiss relative to the granitic, granodioritic and trondhjemitic gneisses. While the large spread in values in individual clusters might reflect real compositional variation, both the restricted sample size and pre- and post-impact alteration effects have likely also contributed to this variability. This is illustrated by Sample M4 IS-2, which is a silicified metadolerite that has SiO_2 = 70 wt% (Table 2, Fig. 9) and an unusual REE pattern (Fig. 10b). The metadolerite

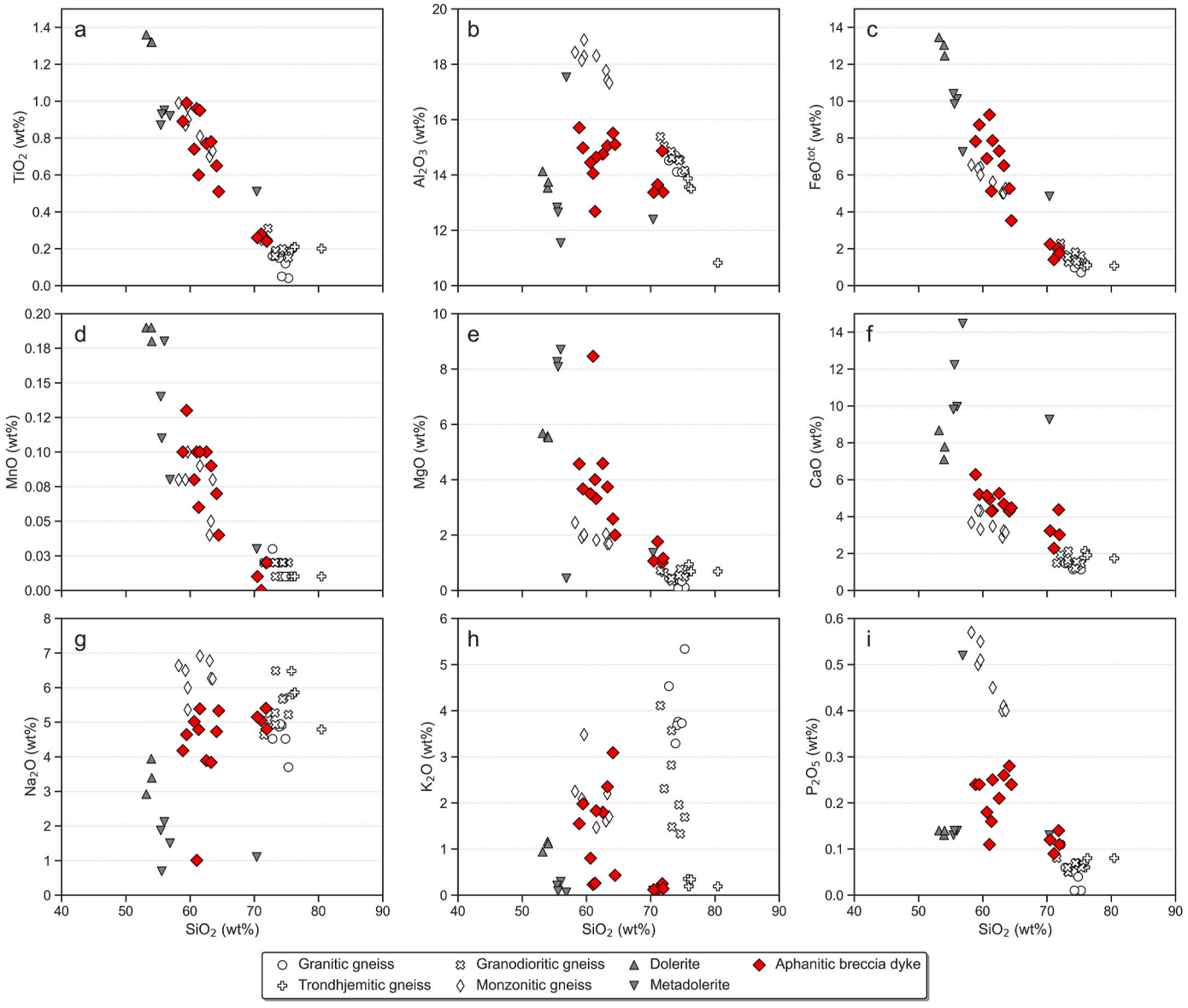


Fig. 9. Major element compositions of granitoid gneisses, dolerites, and aphanitic dykes from the M4 drill core (see Tables 1–3). The oxides compared against SiO_2 include (a) TiO_2; (b) Al_2O_3; (c) total Fe (Fe^{tot}); (d) MnO; (e) MgO; (f) CaO; (g) Na_2O; (h) K_2O; and (i) P_2O_3. Values are presented as weight percent (wt%) oxide.

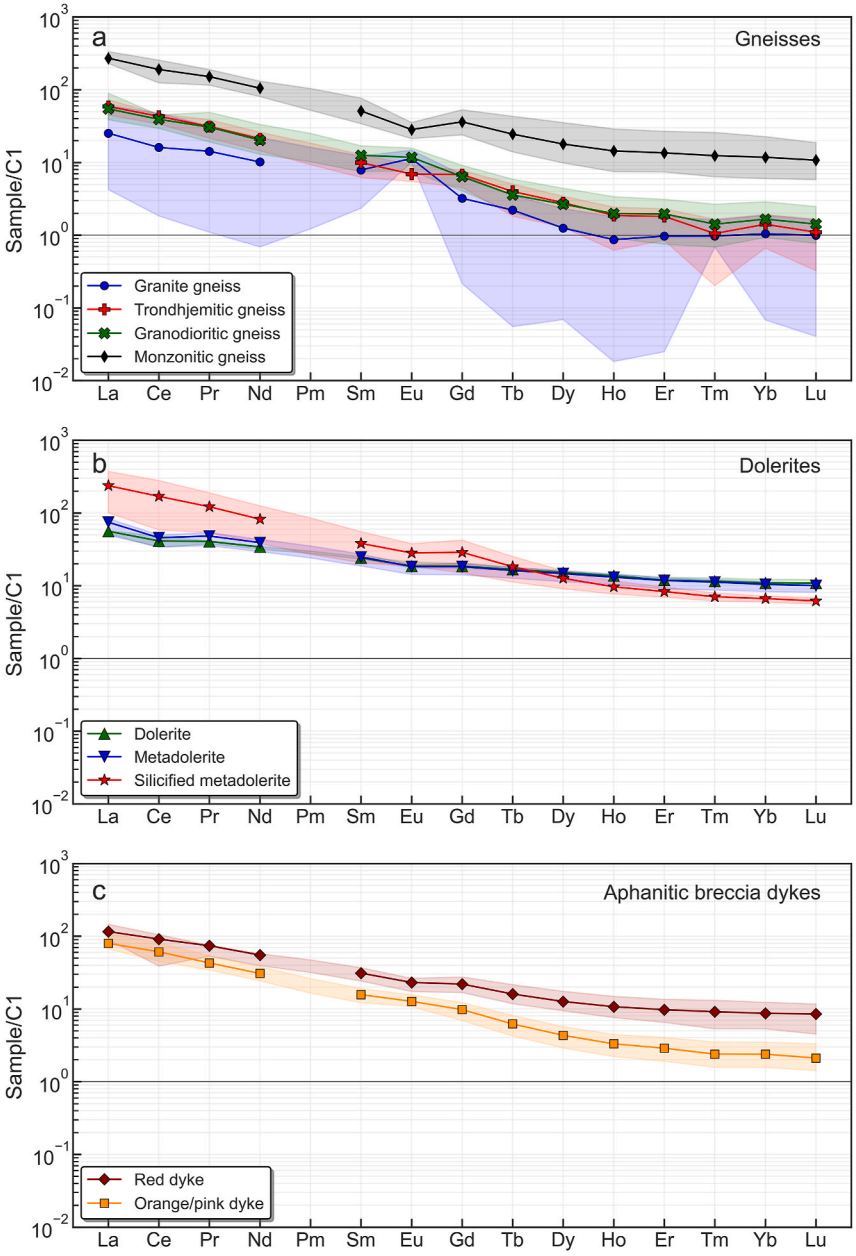


Fig. 10. Chondrite-normalised rare earth element diagram (McDonough and Sun, 1995) showing compositions of rocks from the M4 drill core: (a) granitoid gneisses, (b) dolerites, (c) aphanitic dykes. Lines indicate the median values; the shaded areas represent the range of values. Most granitic gneiss values overlap the field for the granodioritic and trondhjemitic gneisses; the extremely broad range in the granitic gneiss values is caused by two analyses of quartz-plagioclase aplite dykes, which are extremely depleted in most REE.

and aphanitic dyke samples show average LOI values of 1.85 wt% and 4.0 wt% (Tables 2 and 3), respectively, with the latter undoubtedly reflecting the complete post-impact rehydration of the matrices to smectites + zeolites, whereas the former could also reflect a component of pre-impact alteration.

The SiO_2 values for most of the aphanitic dykes (58.8–71.9 wt%) are intermediate between the dolerites (53.1–56.9 wt%, excluding M4 IS-2) and granitic gneisses (71.5–80.4 wt%) but overlap the range for the monzonitic gneiss (58.2–63.5 wt%) (Fig. 9). However, excluding M4 IM-1, the aphanitic dyke sample distribution is bimodal, with four samples overlapping the granitoid gneisses and the remainder – which are more mafic – lying intermediate between the four wallrock clusters. The slightly divergent trend in the more mafic aphanitic dyke analyses away from the granitoid gneiss cluster towards, respectively, the dolerite and metadolerite clusters seen in the TiO_2, FeO^{tot}, and MgO plots is interpreted as reflecting their different locations in the core relative to the respective mafic rock intervals. In terms of Al_2O_3, the felsic (pink/orange) aphanitic dykes have values consistent with some mixing between metadolerite and granitic gneiss, but the more mafic dykes show values similar to, but in some cases slightly higher than, the granitic gneisses and higher than the dolerites (12.7–15.7 wt%; Fig. 9b), which suggests a contribution from the relatively Al_2O_3-enriched monzonitic gneiss. Based on the hydrothermal mineralogy and presence of abundant Ca > Na zeolite veins through the drill core (T. Masiu, pers. comm., 2023), the dykes might be expected to be enriched in CaO and depleted in K_2O and Na_2O; however, while there is overall depletion in K_2O, and Na_2O values show some dispersion, most analyses fall within the compositional quadrilateral defined by the wallrocks, suggesting that the system was relatively isochemical for most elements – at least at the hand sample scale. Sample M4 IM-1, from a dyke intersection from the

metadolerite interval at 176 m depth, shows a composition similar to its metadolerite wallrock (Tables 2 and 3), however, it proved difficult to separate the dyke matrix from brecciated metadolerite clast material owing to the high levels of alteration of both matrix and clasts. Consequently, this analysis may not represent dyke matrix, sensu stricto.

The P_2O_5 content of the aphanitic dykes is elevated relative to both the doleritic and granitic rocks but is still significantly lower than the monzonitic gneiss (Fig. 9i), which is characterised by abundant apatite (Gibson et al., 2022). The lower P_2O_5 content in the felsic (pink/orange) dykes relative to the more mafic dykes suggests that the mafic dykes, which mostly lie between 250 and 300 m depth, preferentially incorporated a monzonitic gneiss component (see Discussion), whereas the pink/orange dykes from shallower levels were derived primarily from the other, apatite-poorer, granitoid lithologies.

7.3. Trace and rare earth elements

The trace element compositions of the gneissic samples show that the monzonitic gneiss has a moderately higher concentration of many trace elements compared to the granitic gneisses (Table 1). The median trace element contents of the other gneisses, and in particular, the granitic and granodioritic gneisses, mostly fall within each other's compositional ranges (Gibson et al., 2022). The metadolerite shows a depletion of large ion lithophile (LIL) elements such as Ba, Cs, Pb, and Rb when compared to the unaltered dolerites, however, the silicified metadolerite exhibits a similar depletion in Ba, Pb, and Rb but a comparative increase in Cs and high-field strength (HFS) elements, such as Sr, Th, and U (Table 2). Differences between the felsic and mafic aphanitic dykes are minor although the mafic dykes have notably lower median concentrations of Ba, Hf, Rb, and Zr (Table 3).

The chondrite-normalised rare earth element (REE) profiles confirm the distinct character of the monzonitic gneiss relative to the other granitoid gneisses (Fig. 10a). The median compositions of the granitic (i.e., non-monzonitic) gneisses are less REE-rich and display a moderate negative slope. The trondhjemitic gneiss, which has a lower LIL content (e.g., Ba and Rb; Table 1), has a small negative Eu anomaly whereas in the granitic and granodioritic gneisses the Eu anomaly is absent to slightly positive (Fig. 10a).

The dolerite and metadolerite samples show very similar, shallow, REE profiles whereas the silicified metadolerite shows a steeper negative profile, with a higher light REE and marginally lower heavy REE content than the former (Fig. 10b). The aphanitic dykes also show relatively shallow REE profiles with no observable Eu-anomaly, with absolute values of REEs intermediate between the granitoid gneisses and doleritic rocks (Fig. 10c). Median compositions for the more mafic (red) dykes, are consistently slightly more enriched than for the felsic (pink/orange) dykes. Comparing this to the petrographic and μXRF results, the evidence points to the voluminous red dykes being derived primarily from the doleritic rocks but with a granitoid gneiss component, and the less voluminous pink/orange dykes reflecting a more strongly granitoid source.

In summary, the major-element data support a somewhat bimodal melt dyke population with silica-rich pink/orange dykes and mafic red dykes. Only the volumetrically minor pink/orange dykes show a composition approaching that of one of the target rock end-members (granitoid cluster), although sample M4 IM-1 may reflect a metadolerite source. In contrast, the more voluminous red dykes show somewhat intermediate compositions between the wallrock endmembers that are consistent with contamination of a principally doleritic melt with a granitic (and possibly also monzonitic) component. The differences in MgO, Al_2O_3, and FeO^{tot} contents of the red dyke in the metadolerite interval between 190 and 230 m versus the red dykes containing dolerite clasts from 260 to 295 m further corroborates a local derivation.

8. Discussion

8.1. Origin of aphanitic breccia dykes in the M4 drill core

The M4 drill core represents the longest intersection through the basement rocks of the MIS; however, the M3 and WF5 cores also contain, respectively, 200 m and 46 m of Archaean basement rocks (Fig. 1b) that also reportedly display mm- to dm-wide, aphanitic to fine-grained breccias (Andreoli et al., 1995, 1999; Hart et al., 1997, 2002; Reimold et al., 1999). Hart et al. (1997) described "veins of fine-grained recrystallized breccia that resembles pseudotachylite" (p. 29) in the WF5 drill core but provided no further details. Reimold et al. (1999) questioned this interpretation, suggesting that multiple types of dyke/vein features appear to be present, but that strong annealing caused by heating attributed to the melt sheet obscures their individual origins. They reported that some dykes contain exotic lithic clasts and that they show ambiguous bulk geochemical results (unpublished data) that failed to adequately discriminate between an in situ versus intrusive/allochthonous derivation of the dykes. From this, Reimold et al. (1999) concluded that options for their genesis other than friction melting – such as shock and/or impact melting – could not be dismissed. With the reported high levels of post-impact annealing, and even localised melting, in the WF5 core, they suggested that some "dykes" could potentially even represent highly annealed cataclasite, rather than true melts. Furthermore, in the M3 core, Hart et al. (2002) and Kenny et al. (2021) noted a sulphide-enriched dyke ~130 m below the base of the melt sheet that they interpreted as a small impact-melt dyke, but no further data concerning it were provided.

Such complexity – and even ambiguity – of origin for impactite breccias in crater basement rocks is reported in other large impact structures (see discussions in Lambert, 1981; Kenkmann et al., 2014; Thompson and Spray, 2017; Spray and Biren, 2021). At Sudbury and Vredefort, the well-exposed crater basements contain both impact melt dykes with widths of up to tens of metres and strike lengths of several kilometres to tens of kilometres, in addition to the largest pseudotachylite dyke occurrences found on Earth. At Vredefort, Martini (1978, 1992) also identified rare mm-wide shock melt dykes containing high-pressure SiO_2 polymorphs and remarked on their overall morphological similarity to pseudotachylites. This and a similar suggestion by Lambert (1981) from the Rochechouart structure, generated considerable debate about the type of nomenclature that should be used for melt breccia dykes in impact structures and how to discriminate shock melts from melts produced purely by frictional heating in impact settings (e.g., Reimold, 1995). This is especially pertinent given the limited likelihood of preservation of high-pressure polymorphs in the face of post-impact heating and/or hydrothermal effects (In more than one case interpretations appear to be based primarily – and maybe even solely – on melt volume). A similar triad of impact-related melt dykes has been identified in the Manicouagan crater basement (Spray and Biren, 2021). At Ries and Rochechouart, impact-melt dyke intrusions into cataclasite have been proposed to explain unusual dykes in the crater basement (Stöffler, 1977; Lambert, 1981).

Notwithstanding the complete replacement of the aphanitic dyke matrices in the M4 drill core by a crypto- to micro-crystalline hydrothermal smectite-zeolite-magnetite paragenesis, the contrast between the texture of this paragenesis and that in the adjacent cataclasite (Fig. 6a) supports a non-clastic – that is, melt – origin for the dykes. This contrast is emphasized by the fact that the dyke margins are locally intimately infolded with adjacent cataclasite, and that cataclasite masses in various stages of disaggregation are common in the dykes, yet the hydrothermal minerals in both retain sharply contrasting grain sizes and textures that point to a fundamental difference in their initial natures. Other circumstantial evidence includes the viscous flow-related laminar and fold features in the dykes, and their intrusive morphologies and high aspect ratios that are consistent with a low-viscosity melt, rather than mobilised cataclasite or ultracataclasite. A friction origin for this melt is

supported by the close spatial and temporal association between the thin aphanitic breccia dykes and cataclasite, including the presence of thin, sub-millimetre, lenses along cataclasite-hosting faults that preserve internal flow features (Fig. 8a) and the classic generation plane + offshoot dyke morphology that is characteristic of tectonic fault-related pseudotachylite (Fig. 8b).

The remaining question is whether the more voluminous dyke intersections in the M4 drill core, which share the same internal characteristics as the thin dykes but for which fine-scale geometric and contact features are obscured, are also pseudotachylite. For instance, Fig. 5d shows one such dyke enclosing granitoid lithic clasts that contain irregular, fracture-controlled, internal aphanitic breccia dykes that are truncated at the clast margins. A similar relationship was described from a clast in an impact-melt dyke in the Vredefort structure by Kovaleva et al. (2018), who interpreted the intra-clast dyke as impact-induced pseudotachylite that appears to have quenched prior to the incorporation of the clast into the impact melt, which only crystallized later owing to its higher initial temperature and larger volume. At a larger scale, Lightfoot et al. (1997) have documented impact melt dykes intruding impact-induced pseudotachylite-cataclasite fault zones in the Sudbury structure. In the M0077A drill core at Chicxulub, an ~100 m thick intersection of melt breccia in the crater basement has been interpreted by De Graaff et al. (2021) as an impact melt dyke injected into a fault in the crater floor during the compression-excavation stage of cratering. They proposed that such melt injections may have played an important lubricating role in central peak formation prior to their quenching, which might potentially have retarded pseudotachylite development.

Given the evidence for mechanical mixing of the melt in the dykes and cataclasite in the M4 drill core, Fig. 11 evaluates an in situ (frictional) versus allochthonous (intrusive impact melt) origin for the more voluminous dykes in the core. In the latter case, the impact melt would have become contaminated by locally derived cataclasite prior to quenching. To test the allochthonous melt hypothesis, we have compared the dyke compositions in the M4 drill core with that of published impact-melt rock compositions from the WF5 drill core (Koeberl and Reimold, 2003). Fig. 11a confirms the bimodal distribution of the M4 aphanitic dykes, with the more felsic cluster showing limited contribution from doleritic or monzonitic sources and the mafic dykes suggesting a more dominant doleritic contribution, with mixing of granitic or monzonitic endmembers. However, in terms of major oxides, the mafic dykes and impact melt plot relatively close to one-another and to the least squares mixing line between the average compositions of the dolerites and granitic gneisses. This result differs from what Spray and Biren (2021) were able to show at Manicouagan, where thin pseudotachylite dykes in fault zones in a large anorthosite block thrust through the melt sheet are compositionally distinct from the surrounding impact-melt rock. This is because the thin dykes show anorthositic compositions consistent with derivation from their anorthosite wallrock, but geochemical analysis shows that the anorthosite was not a source component of the impact melt. Fig. 11a shows that this distinction is not available at Morokweng, where it appears that the lithologies found in the M4 drill core are very similar to those that occur both regionally (Cornell et al., 2018; Gibson et al., 2022) and as clasts in the melt sheet and in its footwall (Andreoli et al., 1999; Reimold et al., 1999; Hart et al., 2002).

The Morokweng impact melt has been suggested to be the result of the homogenous mixing of 50–63% granitic and 35–50% mafic material (Koeberl and Reimold, 2003). This is apparent in Fig. 11a, where the impact melt compositions plot in the middle of the mixing line (primarily between 30% and 60% felsic component) and present as a well constrained compositional array. This corresponds with a large degree of homogenisation and somewhat equal proportions of mixing. In contrast, the compositions of the aphanitic dykes are more variable and appear to be strongly influenced by wallrock lithologies.

The Morokweng impact-melt sheet is, however, noted for its exceptionally high levels of siderophile, platinum group element (PGE) and other trace elements. Andreoli et al. (1999) obtained mean values of 358 ± 73 ppm Cr, 485 ± 161 ppm Ni, and 20 ppb Ir in samples from the M3 drill core, and Koeberl et al. (1997) measured maximum values of 440 ppm Cr, 50 ppm Co, 780 ppm Ni, and 32 ppb Ir in the WF3, WF4 and WF5 cores. McDonald et al. (2001) concluded from PGE concentrations in the melt sheet that the impacting projectile was an ordinary LL chondrite. This was subsequently confirmed by mixing calculations using siderophile element and PGE abundances in samples from the WF5 core by Koeberl and Reimold (2003) who proposed an up to 5% meteoritic component, and by discovery of several altered meteorite fragments in the M3 core (Maier et al., 2006).

In contrast to the ambiguity involving the major element plot (Fig. 11a) and Fig. 11b suggests that the siderophile element content of the mafic aphanitic dykes in the M4 drill core cannot be explained by an impact melt contamination model, unless it was able to achieve ≫50% assimilation of monzonitic gneiss. The conclusion from this modelling is

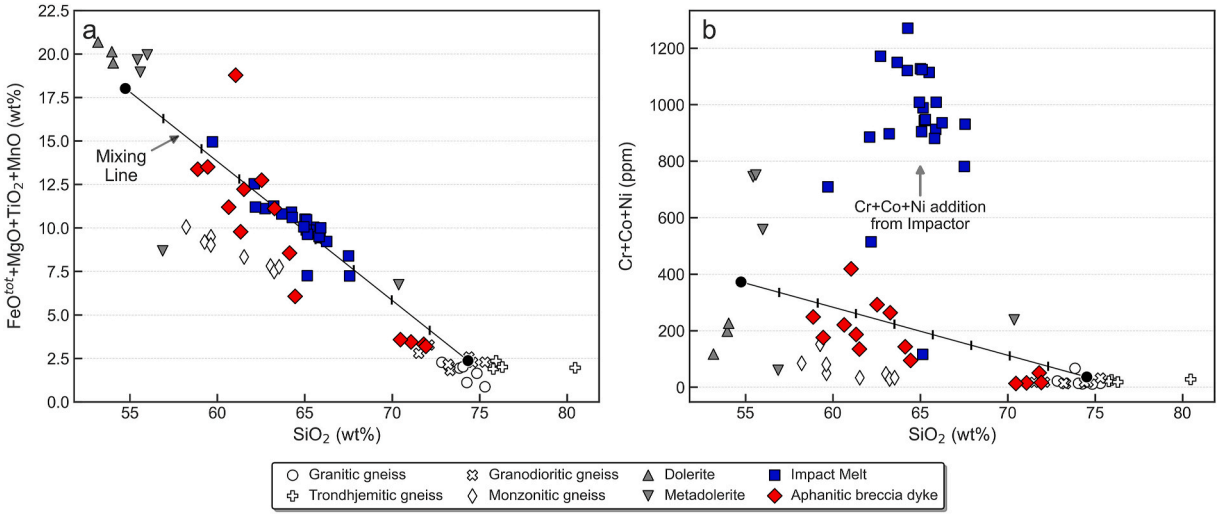


Fig. 11. Comparison of the bulk rock compositional data from M4 drill core samples with impact-melt rock compositional data from the WF5 drill core (Koeberl and Reimold, 2003). (a) FeO^{tot} + MgO + TiO_2+MnO content vs SiO_2; (b) Cr + Co + Ni content vs SiO_2. Black lines represent least squares mixing between the average compositions (represented by black dots) of the mafic (metadolerites and dolerites) and felsic (granitic gneisses excluding the monzonitic gneiss) lithologies in the drill core. For completeness, the highly silicified metadolerite sample M4 IS-2 was included in calculating the mafic average value. Vertical dashes on mixing lines represent 10 % intervals.

that unrealistic levels of assimilation of cataclasite would be needed to produce the M4 dyke compositions from an impact melt, but that the aphanitic dyke compositions can be explained by a more proximal process involving cataclasis and frictional melting of M4 core lithologies.

8.2. Timing of pseudotachylite development during the Morokweng impact

Based on the cumulative evidence, we interpret the aphanitic breccia dykes in the M4 drill core as friction melts formed along faults in par-autochthonous basement. Quartz and feldspar clasts in the dykes contain shock features (Gibson et al., 2024), and the dykes are overprinted by impact-induced hydrothermal alteration, thus bracketing them and the fault network as impact features. The intimate mingling of the melts with cataclasite in the same fault zones (Figs. 5a and 6a,b) prior to quenching suggests a relatively long-lived dynamic stress environment that persisted after initial melt formation. This is contrary to what is typically described in conventional tectonic fault systems, where failure and slip occur and effectively de-stress the rock volume within micro-seconds to seconds, "freezing" fault rock relationships in place. However, such a scenario can be expected in an impact structure where extreme bulk and differential displacements occur over tens to hundreds of seconds following the impact (e.g., Rae et al., 2019).

What is less clear, however, is when exactly this slip occurred within the sequence of crater development (contact and compression stage, excavation stage or modification stage). Spray and Biren (2021) suggested that it is possible that shock melt dyke-fracture systems that form during the contact and compression stage could provide planes of weakness along which post-shock slip movements – and thus friction melting – could subsequently occur. Melosh (1989, 2005) has argued that the intensity of shock pressure would initially favour the development of short, closely spaced shear fractures that, given the proportionality between fracture spacing and slip magnitude, would limit frictional heating. This would limit melt volumes but does not rule out small volumes of pseudotachylite forming during the contact and compression stage of cratering. Furthermore, he suggested that intense vibrations caused by seismic shaking, which is the most widely accepted mechanism for strength degradation in the subcrater basement that allows central uplift and peak-ring formation in craters the size of Morokweng, may temporarily lower frictional sliding resistance between blocks. This could further restrict the development of significant friction melt volumes during the excavation stage of cratering. Conversely, Spray and Biren (2021) suggest that such oscillatory movements could enhance total amount of slip (and thus frictional sliding) over the life of a fault yet result in an apparently negligible final slip displacement owing to slip reversals largely cancelling one-another.

With waning shock pressure and decreasing strain rate as the crater evolves (Rae et al., 2019), slip is expected to become increasingly partitioned into larger, more widely spaced, faults that could thus create more favourable conditions for voluminous pseudotachylite development (Melosh, 2005). This transition is likely to be progressive and occur at slightly different times in different parts of the crater basement, depending on local strain patterns and magnitudes. Optimal conditions would be met during the modification stage but may have commenced as early as the latter parts of the excavation stage (Kenkmann et al., 2014; Rae et al., 2019).

When viewed in conjunction with the concentric magnetic anomalies in the regional geophysical data (Fig. 1), the nature of the rocks in the M4 drill core (i.e., crater basement), their moderately high shock levels and the fact that they are structurally elevated by a minimum of ~800 m relative to the base of the melt sheet in the central holes led Gibson et al. (2024) to propose that the M4 drill core represents a section through the partially eroded structural peak ring of the MIS. This means that, during the crater modification stage, the rock volume would have experienced strong vertical upward translation, initially under constrictional strain conditions, followed by later collapse and centrifugal translation. Gibson et al. (2024) drew comparisons to the M0077A drill core through the Chicxulub peak ring which also displays moderately high shock levels, closely spaced shear faults, cataclasite and pseudotachylite (Riller et al., 2018). However, there is an important difference in that Riller et al. (2018) describe most shear faults in the M0077A drill core as having a normal sense of slip and thus attribute their origin to the final stages of centrifugally directed extensional collapse of the upper parts of the outer toe of the central uplift. Conversely, the faults in the M4 drill core display a reverse slip sense. The lack of precise orientation of the M4 drill core precludes a more specific interpretation of slip vergence; however, both modelling (e.g., Rae et al., 2019) and observations from other central uplifts (Wieland et al., 2005; Kenkmann et al., 2011; Manzi et al., 2021) document constrictional strain (tangential shortening) during the initial stages of central uplift rise. Jahn and Riller (2015) have further suggested that the extreme rotations occurring in large central uplifts could re-orient initially centripetally dipping listric normal faults related to collapse of the transient cavity to centrifugal dips (and, thus, reverse the apparent slip sense). Finally, Riller et al. (2018) noted some reverse-slip faults in the deeper part of the M0077A drill core that might fit this model or, alternatively, could reflect underthrusting of the collapsing crater rim beneath the overlying outward-collapsing central uplift. The evidence of more than 1 km of erosion in the MIS would support the M4 section representing correspondingly deeper levels of a peak ring volume than found in the M0077A core. Alternatively, based on modelled internal strain patterns in central uplift volumes, it is also possible that reverse slip may be characteristic of volumes closer to the centre of the impact structure (e.g., Rae et al., 2019). If this holds for the faults in the M4 drill core, then it may mean that they formed relatively late during the modification stage. This may have implications for both the rheology of the central uplift and size estimates of the MIS.

8.3. Implications for melting mechanisms

The small-volume pink/orange melt breccia dykes in the M4 drill core display compositions that are close to, but slightly more mafic than, their granitoid wallrocks. This relationship is consistent with Spray's (1992, 2010) findings that the composition of a pseudotachylite melt typically deviates from that of the wallrocks towards that of mechanically weak minerals with internal cleavage and/or the lowest melting temperatures, such as hydrous ferromagnesian silicates (chlorite, biotite, and amphibole) and aluminosilicates like feldspars. The release of H_2O from the hydrous minerals may also assist in catalysing further melting of anhydrous phases. However, the compositions of the more voluminous red to reddish-brown dykes are more felsic than the dolerites. Given the high levels of hydrothermal alteration, it is impossible to tell whether this is a function of direct melting of alkali-feldspars and quartz by friction and then mixing of separate mafic and felsic friction melts, or suprasolidus heating of felsic mineral and lithic clasts after their incorporation within a mafic melt, causing them to melt as well. The evidence of mafic dykes inside the granitoid gneisses, and their high aspect ratio suggest that the mafic melts may have had low initial viscosities and, thus, were able to intrude significant distances before quenching. Intrusion into cataclasite-filled fractures would have offered large amounts of already finely comminuted felsic clast material that could have been both mechanically dispersed within the melt and subjected to melting.

Given the dominance of voluminous red, mafic, dykes in the M4 drill core and the microscopic and geochemical evidence that they are contaminated by a felsic component, one option is that slip was preferentially localised along the intrusive mafic dyke contacts into the granitoid gneisses. This would have allowed the selective melting of ferromagnesian minerals and plagioclase in the metadolerite/dolerite, and possible subsidiary melting of alkali feldspars and the limited amounts of biotite in the granitoid gneisses. Flow-assisted mixing of the end-member melts could then explain the observed compositional and

textural features. The second model is that voluminous mafic melts from the dolerites entrained and partially assimilated granitoid-derived cataclasite through intrusion and infolding. Infolding is favoured, as intrusion into an incohesive cataclasite might be quite difficult, although some evidence for the latter exists. While some features are suggestive of relatively passive intrusion of melts, an acceptable source of intrusive push could come from strong and complex block movements during and following faulting.

9. Conclusions

The millimetre- to metre-thick aphanitic, clast-bearing dykes in the M4 drill core of the Morokweng impact structure show structural association with fault-hosted cataclasite and compositions consistent with derivation from their wallrocks. Comparison of dyke geochemistry with the impact-melt rock found in adjacent drill cores does not support them being contaminated intrusions of impact melt into the Morokweng crater basement; instead, they are interpreted as friction melts (pseudotachylite) formed during high strain rate reverse-slip faulting associated with the cratering event. Dyke emplacement and mechanical incorporation of significant volumes of incohesive cataclasite prior to quenching of the melts appear to have been aided by ongoing slip, or reactivation, of cataclasite zones caused by the complex movements during crater modification within the peak ring volume. Subsequent impact-induced hydrothermal alteration led to devitrification of the dyke matrices to smectites and zeolites, with negligible open system behaviour.

CRediT authorship contribution statement

Roger L. Gibson: Investigation, Conceptualization, Methodology, Supervision, Visualization, Writing – original draft. **S'lindile S. Wela:** Investigation, Methodology, Writing – original draft. **Leonidas C. Vonopartis:** Formal analysis, Software, Writing – original draft. **Marco A.G. Andreoli:** Conceptualization, Supervision, Writing – review & editing.

Declaration of competing interest

No conflict of interest statement.

Data availability

Data will be made available on request.

Acknowledgements

Research access to the M4 core by Business Venture Investments no. 33 (Pty) Ltd is gratefully acknowledged. This work is based on research supported in part by the National Research Foundation of South Africa Grant SRUG200503519568 to RG. MA acknowledges prior financial support from the NRF Rated Researcher Programme, and SW received a Wits University Postgraduate Merit Award. Geochemical results from six samples from an unpublished Honours project by L. Luruli are included in the dataset. M. Patchappa (XRF and ICP-MS analysis), C. Majola (thin sections) and Igor Tonzetic (μXRF) are thanked for technical assistance. Constructive reviews by A. Wittmann and C. Koeberl are gratefully acknowledged.

References

Andreoli, M.A.G., Ashwal, L.D., Hart, R.J., Smith, C.B., Webb, S.J., Tredoux, M., Gabrielli, F., Cox, R., Hambleton-Jones, B.B., 1995. The Impact Origin of the Morokweng Ring Structure, Southern Kalahari, South Africa. Geological Society of South Africa Centennial Geocongress, Johannesburg, pp. 541–544. Extended Abstract I.

Andreoli, M.A.G., Ashwal, L.D., Hart, R.J., Huizenga, J.M., 1999. A Ni and PGE-enriched quartz norite impact melt complex in the Late Jurassic Morokweng impact structure, South Africa. In: Dressler, B.O., Sharpton, V.L. (Eds.), Large Meteorite Impacts and Planetary Evolution II, vol. 339. Geological Society of America, pp. 91–108. Special Paper.

Biren, M.B., Spray, J.G., 2011. Shock veins in the central uplift of the Manicouagan impact structure: context and genesis. Earth Planet Sci. Lett. 303, 310–322.

Cornell, D.H., Minnaar, H., Frei, D., Kristoffersen, M., 2018. Precise microbeam dating defines three Archaean granitoid suites at the southwestern margin of the Kaapvaal Craton. Precambrian Res. 304, 21–38.

Corner, B., Reimold, W.U., Brandt, D., Koeberl, C., 1997. Morokweng impact structure, Northwest Province, South Africa: geophysical imaging and some preliminary shock petrographic studies. Earth Planet Sci. Lett. 146, 351–364.

De Graaff, S.J., Kaskes, P., Dehais, T., Goderis, S., et al., 2021. New insights into the formation and emplacement of impact melt rocks within the Chicxulub impact structure, following the 2016 IODP-ICDP Expedition 364. GSA Bull. 134, 293–315.

French, B.M., 1998. Traces of Catastrophe: A Handbook of Shock-Metamorphic Effects in Terrestrial Meteorite Impact Structures. Lunar and Planetary Institute Contribution No. 954. Lunar and Planetary Institute, Houston, Texas, p. 120.

Gibson, R.L., Wela, S.S., Bybee, G.M., Frei, D., Andreoli, M.A.G., 2022. Granitoid gneisses of the Morokweng impact structure: implications for Neoarchaean evolution of the western Kaapvaal craton. Lithos 426–427, 106793. https://doi.org/10.1016/j.lithos.2022.106793.

Gibson, R.L., Wela, S.S., Rae, A.S.P., Andreoli, M.A.G., 2024. Shock petrographic and numerical modeling constraints on the morphology and size of the Morokweng impact structure, South Africa, accepted to. Meteoritics Planet Sci.

Grieve, R.A.F., Dence, M.R., Robertson, P.B., 1977. Cratering processes: as interpreted from the occurrence of impact melts. In: Roddy, D.J., Pepin, R.O., Merrill, R.B. (Eds.), Impact and Explosion Cratering. Pergamon Press, New York, pp. 791–814.

Hall, A.L., Molengraaff, G.A.F., 1925. The Vredefort Mountain Land in the Southern Transvaal and the Northern Orange Free State, vol. 24. Koninklijke Akademie van Wetenschappen, Amsterdam, p. 183. Verbandelingen.

Hart, R.J., Andreoli, M.A.G., Tredoux, M., Moser, D., Ashwal, L.D., Eide, E., Webb, S.J., Brandt, D., 1997. Late Jurassic age for the Morokweng impact structure, southern Africa. Earth Planet Sci. Lett. 147, 25–35.

Hart, R.J., Cloete, M., McDonald, I., Carlson, R.W., Andreoli, M.A.G., 2002. Siderophile-rich inclusions from the Morokweng impact melt sheet, South Africa: possible fragments of a chondritic meteorite. Earth Planet Sci. Lett. 198, 49–62.

Henkel, H., Reimold, W.U., Koeberl, C., 2002. Magnetic and gravity model of the Morokweng impact structure. J. Appl. Geophys. 49, 129–147.

Jahn, A., Riller, U., 2015. Kinematics of Large Terrestrial Impact Crater Formation Inferred from Structural Analysis and Three-Dimensional Block Modeling of the Vredefort Dome, vol. 518. Special Papers Geological Society of America, South Africa, pp. 85–97.

Kenkmann, T., Vasconcelos, M.A., Crosta, A.P., Reimold, W.U., 2011. The complex impact structure Serra da Cangalha, Tocantins State, Brazil. Meteoritics Planet Sci. 46, 875–889.

Kenkmann, T., Poelchau, M.H., Wulf, G., 2014. Structural geology of impact craters. J. Struct. Geol. 62, 156–182.

Kenny, G.G., Harrigan, C.O., Schmitz, M.D., Crowley, J.L., Wall, C.J., Andreoli, M.A.G., Gibson, R.L., Maier, W.D., 2021. Timescales of impact melt sheet crystallization and the precise age of the Morokweng impact structure, South Africa. Earth Planet Sci. Lett. 567, 117013 https://doi.org/10.1016/j.epsl.2021.117013.

Koeberl, C., Reimold, W.U., 2003. Geochemistry and petrography of impact breccias and target rocks from the 145 Ma Morokweng impact structure, South Africa. Geochem. Cosmochim. Acta 67, 1837–1862.

Koeberl, C., Armstrong, R.A., Reimold, W.U., 1997. Morokweng, South Africa: a large impact structure of Jurassic-Cretaceous boundary age. Geology 25, 731–734.

Koeberl, C., Peucker-Ehrenbrink, B., Reimold, W.U., Shukolyukov, A., Lugmair, G.W., 2002. Comparison of the osmium and chromium isotopic methods for the detection of meteoritic components in impactites: examples from the Morokweng and Vredefort impact structures, South Africa. In: Koeberl, C., MacLeod, K.G. (Eds.), Catastrophic Events and Mass Extinctions: Impacts and beyond, vol. 618. Geological Society of America Special Paper, pp. 607–618.

Kovaleva, E., Huber, M.S., Roelofse, F., Tredoux, M., Praekelt, H., 2018. Pseudotachylite vein hosted by a clast in the Vredefort Granophyre: characterization, origin, and relevance. S. Afr. J. Geol. 121, 51–68.

Lambert, P., 1981. Breccia dikes: geological constraints on the formation of complex craters. In: Schultz, P.H., Merrill, R.B. (Eds.), Multi-Ring Basins. Pergamon Press, New York, pp. 59–78.

Lightfoot, P.C., Doherty, W., Farrell, K., Keays, R.R., Moore, M., Pekeski, D., 1997. Geochemistry of the Main Mass, Sublayer, Offsets, and Inclusions from the Sudbury Igneous Complex. Ontario Geological Survey, Ontario, p. 231. Open File Report 5959.

Maier, W.D., Andreoli, M.A.G., McDonald, I., Higgins, M.D., Boyce, A.J., Shukolyukov, A., Lugmair, G.W., Ashwal, L.D., Graser, P., Ripley, E.M., Hart, R.J., 2006. Discovery of a 25 cm asteroid clast in the giant Morokweng impact crater, South Africa. Nature 441, 203–206.

Manzi, S., Gibson, R.L., Tshibubudze, A., 2021. Dynamics of collapse of an impact central uplift: evidence from folds and faults in the collar of the Vredefort Dome, South Africa. In: Reimold, W.U., Koeberl, C. (Eds.), Large Meteorite Impacts and Planetary Evolution VI, vol. 550. Geological Society of America Special Paper, pp. 585–606.

Martini, J.E.J., 1978. Coesite and stishovite in the Vredefort dome, South Africa. Nature 272, 715–717.

Martini, J.E.J., 1992. The nature, distribution and genesis of the coesite and stishovite associated with pseudotachylite of the Vredefort Dome, South Africa. Earth Planet Sci. Lett. 103, 285–300.
McDonald, I., Andreoli, M.A.G., Hart, R.J., Tredoux, M., 2001. Platinum-group elements in the Morokweng impact structure South Africa: evidence for the impact of a large ordinary chondrite projectile at the Jurassic-Cretaceous boundary. Geochem. Cosmochim. Acta 65, 299–309.
McDonough, W.F., Sun, S.S., 1995. The composition of the Earth. Chem. Geol. 120, 223–253.
Melosh, H.J., 1989. Impact Cratering: A Geologic Process. Oxford University Press, New York, p. 245.
Melosh, H.J., 2005. The mechanics of pseudotachylite formation in impact events. In: Koeberl, C., Henkel, H. (Eds.), Impact Tectonics, Impact Studies Series, vol. 1. Springer, Heidelberg, pp. 55–80.
Osinski, G.R., Grieve, R.A.F., Marion, C., Chanou, A., 2013. Impact melting. In: Osinski, G.R., Pierazzo, E. (Eds.), Impact Cratering: Processes and Products. Blackwell Publishing Ltd, UK, pp. 126–145.
Rae, A.S.P., Collins, G.S., Poelchau, M., IODP-ICDP Expedition 364 Scientists, 2019. Stress-strain evolution during peak-ring formation: a case study of the Chicxulub impact structure. J. Geophys. Res.: Planets 124, 396–417. https://doi.org/10.1029/2018JE005821.
Reimold, W.U., 1995. Pseudotachylite in impact structures – generation by friction melting and shock brecciation? A review and discussion. Earth Sci. Rev. 39, 247–264.
Reimold, W.U., Gibson, R.L., 2005. 'Pseudotachylites' in large impact structures. In: Koeberl, C., Henkel, H. (Eds.), Impact Tectonics, Impact Studies Series, vol. 6. Springer, Heidelberg, pp. 1–53.
Reimold, W.U., Koeberl, C., Brandstatter, F., Armstrong, R.A., Bootsman, C., 1999. The Morokweng impact structure, South Africa: geologic, petrographic and isotopic results, and implications for the size of the structure. In: Dressler, B.O., Sharpton, V. L. (Eds.), Large Meteorite Impacts and Planetary Evolution II, vol. 339. Geological Society of America Special Paper, pp. 61–90.
Riller, U., Poelchau, M.H., Rae, A.S.P., Schulte, F.M., Collins, G.S., Melosh, H.J., Expedition 364 Science Party, IODP-ICDP, 2018. Rock fluidization during peak-ring crater formation. Nature 562, 511–518. https://doi.org/10.1038/s41586-018-0607-z.
Sibson, R.H., 1975. Generation of pseudotachylyte by ancient seismic faulting. Geophys. J. Roy. Astron. Soc. 43, 775–794.
Spray, J.G., 1992. A physical basis for the frictional melting of some rock-forming minerals. Tectonophysics 204, 205–221.
Spray, J.G., 2010. Frictional melting processes in planetary materials: from hypervelocity impact to earthquakes. Annu. Rev. Earth Planet Sci. 38, 221–254. https://doi.org/10.1146/annurev.earth.031208.100045.
Spray, J.G., Biren, M.B., 2021. Distinguishing friction- from shock-generated melt products in hypervelocity impact structures. In: Reimold, W.U., Koeberl, C. (Eds.), Large Meteorite Impacts and Planetary Evolution VI, vol. 550. Geological Society of America Special Paper, pp. 147–170.
Stöffler, D., 1977. Research drilling Nördlingen 1973: polymict breccias, crater basement, and cratering model of the Ries impact structure. Geol. Bavarica 75, 443–458.
Thompson, L.M., Spray, J.G., 2017. Dynamic interaction between impact melt and fragmented basement at Manicouagan: the suevite connection. Meteoritics Planet Sci. 52, 1300–1329.
Wela, S.S., 2017. A lithological, petrographic and geochemical investigation of the M4 borehole core. Morokweng Impact Structure, South Africa. MSc Dissertation (Unpublished). University of the Witwatersrand, p. 385.
Wieland, F., Gibson, R.L., Reimold, W.U., 2005. Structural analysis of the collar of the Vredefort dome, South Africa – significance for impact-related deformation and central uplift formation. Meteoritics Planet Sci. 40, 1537–1554.
Wilson, A.H., 2012. A chill sequence to the Bushveld Complex: insight into the first stage of emplacement and implications for the parental magmas. J. Petrol. 53, 1123–1168.